Elevated gas hydrate saturation within silt and silty clay sediments in the Shenhu area, South China Sea

Xiujuan Wang,[1] Deborah R. Hutchinson,[2] Shiguo Wu,[1] Shengxiong Yang,[3] and Yiqun Guo[3]

Received 24 August 2010; revised 14 February 2011; accepted 3 March 2011; published 25 May 2011.

[1] Gas hydrate saturations were estimated using five different methods in silt and silty clay foraminiferous sediments from drill hole SH2 in the South China Sea. Gas hydrate saturations derived from observed pore water chloride values in core samples range from 10 to 45% of the pore space at 190–221 m below seafloor (mbsf). Gas hydrate saturations estimated from resistivity (R_t) using wireline logging results are similar and range from 10 to 40.5% in the pore space. Gas hydrate saturations were also estimated by *P* wave velocity obtained during wireline logging by using a simplified three-phase equation (STPE) and effective medium theory (EMT) models. Gas hydrate saturations obtained from the STPE velocity model (41.0% maximum) are slightly higher than those calculated with the EMT velocity model (38.5% maximum). Methane analysis from a 69 cm long depressurized core from the hydrate-bearing sediment zone indicates that gas hydrate saturation is about 27.08% of the pore space at 197.5 mbsf. Results from the five methods show similar values and nearly identical trends in gas hydrate saturations above the base of the gas hydrate stability zone at depths of 190 to 221 mbsf. Gas hydrate occurs within units of clayey slit and silt containing abundant calcareous nannofossils and foraminifer, which increase the porosities of the fine-grained sediments and provide space for enhanced gas hydrate formation. In addition, gas chimneys, faults, and fractures identified from three-dimensional (3-D) and high-resolution two-dimensional (2-D) seismic data provide pathways for fluids migrating into the gas hydrate stability zone which transport methane for the formation of gas hydrate. Sedimentation and local canyon migration may contribute to higher gas hydrate saturations near the base of the stability zone.

Citation: Wang, X., D. R. Hutchinson, S. Wu, S. Yang, and Y. Guo (2011), Elevated gas hydrate saturation within silt and silty clay sediments in the Shenhu area, South China Sea, *J. Geophys. Res.*, *116*, B05102, doi:10.1029/2010JB007944.

1. Introduction

[2] In June 2007, eight sites on the continental margin along the north slope of the South China Sea (SCS) were drilled to study gas hydrate, following about ten years of seismic exploration. Sites SH2, SH3 and SH7 in water depths of 1105 to 1423 m (Figure 1) contained gas hydrate in recovered core samples [*Zhang et al.*, 2007; *Yang et al.*, 2008; *Wu et al.*, 2008]. Sites SH1 and SH5 did not recover gas hydrate samples; and sites SH4, SH6 and SH8 were drilled for logging, i.e., without core samples. Considerable seismic analysis and interpretation of the spatial distribution of gas hydrate preceded drilling [*S.G. Wu et al.*, 2009; *N.Y. Wu et al.*, 2009]. The drilling expedition, GMGS-1, was successfully completed by Guangzhou Marine Geological Survey (GMGS), China Geological Survey (CGS) and the Ministry of Land and Resources of P. R. China [*Zhang et al.*, 2007]. Wireline logging, in situ temperature measurements, pore water sampling and pressurized and nonpressurized coring were used to identify gas hydrates. Site SH2 contained the most abundant evidence for the occurrence of gas hydrate.

[3] When sediment samples containing gas hydrate are brought to surface conditions, gas hydrate dissociates, generating fresh water and gas. Pore water extracted from samples of a gas hydrate–bearing layer will be fresher than the in situ water and the decrease of chlorinity and salinity can be used to estimate gas hydrate saturations [*Yuan et al.*, 1996; *Paull and Ussler*, 1997; *Riedel et al.*, 2006]. Gas hydrate saturations were calculated from pore water freshening at sites SH2, SH3 and SH7 [*Yang et al.*, 2008; *Zhang et al.*, 2007], but these calculations are limited to locations in which core samples were recovered. Gas hydrate saturation estimated from wireline logging data, when calibrated to saturation estimated from pressure core degassing, can provide more continuous and higher vertical resolution than measurements from widely spaced core samples [*Hadley et al.*, 2008].

[4] In addition to chloride anomaly methods, quantifying gas hydrate saturations can also be done using downhole logs from measurements of electrical resistivity, acoustic

[1]Key Laboratory of Marine Geology and Environment and Institute of Oceanology, Chinese Academy of Sciences, Qingdao, China.
[2]U.S. Geological Survey, Woods Hole, Massachusetts, USA.
[3]Guangzhou Marine Geological Survey, MLR, Guangzhou, China.

0148-0227/11/2010JB007944

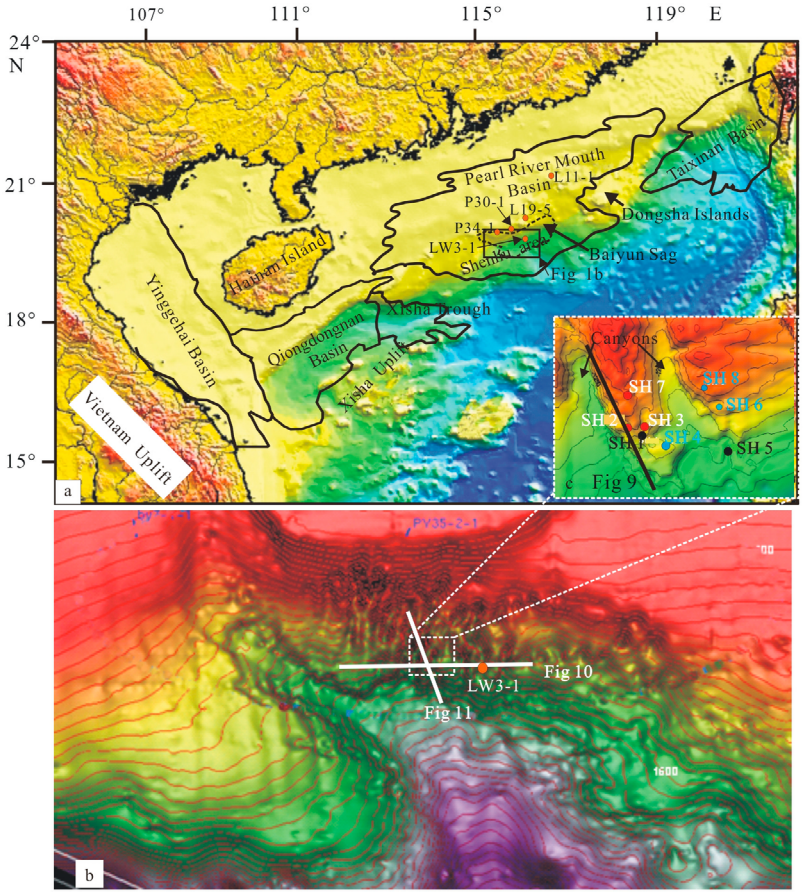

Figure 1. (a) Areas of gas hydrate exploration in the northern part of the South China Sea: Taixinan basin, Pearl River Mouth basin, Xisha trough, and Qiongdongnan basin. (b) Bathymetric map of the gas hydrate study area (location shown by rectangle in Figure 1a), showing the many canyons developed on the north side of the major canyon that crosses the area [*Zhu et al.*, 2010]. Locations of two seismic lines are shown by the white lines. (c) Enlargement of the drilling showing the drilling sites (red dots, gas hydrate samples obtained at SH2, SH3, and SH7; black dots, no gas hydrate samples obtained at SH1 and SH5; blue dots, unknown, no samples were taken at SH4, SH6, and SH8). Seismic line A (Figure 9) crosses drill site SH2; seismic line B (Figure 10) crosses the LW3–1 gas field (Figure 1b); and seismic line C (Figure 11) crosses SH7 and SH3.

velocity, density, and formation porosity. Resistivity methods utilize Archie's law and estimate gas hydrate saturations with Archie parameters and the saturation exponent in isotropic and anisotropic reservoirs [e.g., *Collett and Ladd*, 2000; *Lee and Collett*, 2009a]. Various theoretical, semi-empirical, and ad hoc models also have been proposed to relate gas hydrate saturation to compressional velocity, such as those of *Wood et al.* [1994], *Yuan et al.* [1996], and *Korenaga et al.* [1997], which used *Wyllie et al.*'s [1958] time average equation to estimate gas hydrate saturation after the velocity structure is obtained from seismic data. *Lee et al.* [1993, 1994, 1996] used a weighted equation, *Lee* [2002] used the Biot-Gassmann equation, and *Helgerud et al.* [1999] used effective medium theory (EMT), for relating the velocity of gas hydrate–bearing sediments to gas hydrate saturation. *Lee and Collett* [2009a] used the *P* and *S* wave velocities in anisotropic media to estimate gas hydrate saturation in fractured sediments. The three phase Biot-type equation (TPBE) is developed to compute elastic velocities through gas hydrate–bearing sediments based on different bulk and shear moduli calculations [*Carcione et al.*, 2005; *Tinivella and Lodolo*, 2000; *Carcione and Tinivella*, 2000]. A simplified three phase equation (STPE) proposed by *Lee and Waite* [2008] was intended to describe load-bearing gas hydrate distribution in sands.

[5] In this paper, we use borehole data from GMGS-1 and multichannel seismic data acquired by GMGS in 2006 at Shenhu area. We calculate gas hydrate saturation using resistivity and *P* wave velocities obtained from wireline logging (using EMT and STPE models) assuming isotropic gas hydrate–bearing sediments at site SH2, and chloride concentrations from cores. Gas hydrate saturations estimated from *P* wave velocities and resistivity are based on the density, density porosity and material properties determined from the cored sediments at this site under the assumption that the reservoir is isotropic. We compare the gas hydrate saturations estimated from these different methods to understand the differences among them. Multichannel seismic *P* wave velocity estimated from Constrained Sparse Spike Inversion (CSSI) was used to provide information away from the well.

At the well location, the *P* wave velocity from seismic data fit well with the log data. The vertical and lateral distribution of gas hydrate is investigated using inverted compressional velocities from seismic data together with information from samples at site SH3 and SH7. A model for the occurrence of gas hydrate with high saturations in the fine-grained sediments in Shenhu area, South China Sea is proposed.

2. Geological Setting

[6] The north slope of the South China Sea (SCS) is a passive continental margin formed prior to or during the Middle Oligocene–Early Miocene opening of the so-called central basin (32–17 Ma) [*Briais et al.*, 1993; *Clift et al.*, 2002]. Since 1999, high-resolution multichannel two-dimensional and three-dimensional seismic surveys have been carried out for gas hydrate resource research in the northern South China Sea [*Zhang et al.*, 2002] by the Guangzhou Marine Geological Survey (GMGS). Bottom simulating reflections (BSRs) have been identified in the Taixinan basin [*Wang et al.*, 2006], the Pearl River Mouth (PRM) basin [*Zhang et al.*, 2007; *Yang et al.*, 2008; *Wu et al.*, 2008; *Guo et al.*, 2004], the Xisha Trough [*Wu et al.*, 2005] and Qiongdongnan basin [*Wang et al.*, 2010] (Figure 1). The PRM basin, located on the northern continental shelf of the SCS, is a Cenozoic rift basin; its structural evolution can be divided into two stages: an Eocene–Oligocene rift and a Neogene–Quaternary postrift thermal subsidence phase [*Ru and Pigott*, 1986; *Huang et al.*, 2003]. During the Eocene rifting stage, lacustrine facies mudstones were deposited that are the main hydrocarbon source rocks in this basin. The lower Oligocene deposits were composed mainly of fluvial, swamp, and shallow lacustrine sandstones interbedded with black shales and thin coal seams [*Zhu et al.*, 2009]. Gas fields near site SH2 (e. g., P34–1, P30–1, L19–5 and L11–1, Figure 1a) drilled in shallow water depth and gas field LW3–1 in the deep water are believed to share the same source rocks. Bright spots and gas chimneys are observed in the Miocene sequences on seismic profiles for oil and gas exploration through the deep water area. The gas migrated from the lower Oligocene level by faults and gas chimneys [*Pang et al.*, 2006]. The average thermal gradient is about 36°C/km but can locally reach 50°C/km in the area around site SH2 [*Zhu et al.*, 2009].

[7] Even though the boreholes were not cored continuously during GMGS expedition 1, three important geologic ages are dated from calcareous nannofossils at site SH2 [*Chen et al.*, 2009]. The base of Pleistocene (1.8 Ma) is at about 60 mbsf and the base of the Pliocene (5.3 Ma) is at about 150 mbsf at site SH2 (Figure 2). There are no sharp changes of lithology after the Pleistocene, as indicated by the gamma ray log at site SH2 (Figure 2). X-ray diffraction of core sediment samples indicated that the sediment components consisted of detrital components, clay minerals and carbonate minerals. The detrital minerals mainly included quartz, feldspar, mica and pyrite. Most of carbonate mineral is calcite, with a minor component of dolomite [*Lu et al.*, 2009].

[8] Unlike areas where high-saturation gas hydrates have been recovered from coarse-grained reservoirs such as Mallik in Canada [*Dallimore and Collett*, 2005; *Dallimore et al.*, 1999], Nankai Trough offshore Japan [*Uchida and Takashi*, 2004], and southern Hydrate Ridge offshore Oregon [*Tréhu et al.*, 2004, 2003, 2006], the gas hydrates recovered from SH2 occurred in fine-grained sediments with the maximum sand content of 2% and silt content ranging from 70 to 80% [*Chen et al.*, 2010], similar to fine-grained clay and silt of the Blake Ridge where low saturations occur except in discrete layers of higher saturations in relatively coarse-grained sediments or thin sand layers [e.g., *Ginsburg et al.*, 2000; *Paull and Matsumoto*, 2000]. Sediments drilled in the SCS have higher saturations as determined from pore water analyses than have previously been seen in marine settings in the absence of sand lithologies [*Yang et al.*, 2008; *Zhang et al.*, 2007]. Analysis of the discontinuous core samples from drill sites SH2 (Figure 2) showed that gas hydrate–bearing sediments consisted of calcareous nannofossils silt and clayey silt and that the foraminifera and calcareous nannofossils were abundant and diatoms and radiolarians also occur in the gas hydrate–bearing sediments at 190 to 221 m below the seafloor (mbsf). Siliceous nannofossils (diatoms and radiolarians) were most abundant in the shallowest sediments below the seafloor (about 24 m) [*Chen et al.*, 2009].

3. Data and Methods

[9] The site SH2 was drilled in water depths of about 1230 m within the Baiyun sag, Shenhu area, the Pearl River Mouth basin (PRMB) (Figure 1). Well logs were acquired at five of the eight drilled sites, which are separated by distances ranging from 200 m to 6 km. The well logs at site SH2 include natural gamma ray, gamma density, resistivity, temperature, *P* wave velocity and caliper log. The caliper logs show bad borehole conditions at depths up to 70 mbsf where logging data may not be reliable. The density, *P* wave velocity and gamma ray change greatly in depths from seafloor to ~50 mbsf because of the bad borehole conditions, so gas hydrate saturations have not been estimated in this shallowest part of the drill hole. The *P* wave velocity profile was obtained using a constrained sparse spike inversion package (Jason Geoscience Workbench, 2003) to study the spatial distribution of gas hydrate. Porosity estimates derived from recovered cores and the terrigenous components and calcite content estimated from X ray diffraction are also used in the study [*Chen et al.*, 2009]. Grain size contents of core samples tested from Laser Particle Size Analyzer indicated that core sediments mainly included silt (0.004~0.063 mm) and clay (0.004~0.001 mm) with minor sand (>0.063 mm) (Figure 2).

[10] The 3-D seismic line A and the multichannel 2-D seismic lines B and C through site SH2 were used for this study. The seismic profiles were shot using a 3000 m long streamer with 240 channels (trace interval 12.5 m) and a tuned air gun source with a total volume of 8 × 20 $inch^3$ shooting every 25 m. The sampling interval was 1 ms. The streamer depth was 8 m and the source depth 5 m. The 3-D seismic data, covering an area approximately 9.3 km × 7 km, were processed with a bin spacing in the in-line and cross-line directions of 12.5 m and 25 m, respectively.

4. Results

4.1. Gas Hydrate Saturations

4.1.1. Saturation From Chloride Concentration

[11] Chloride concentrations were measured on core samples that were primarily from depths greater than 140 m

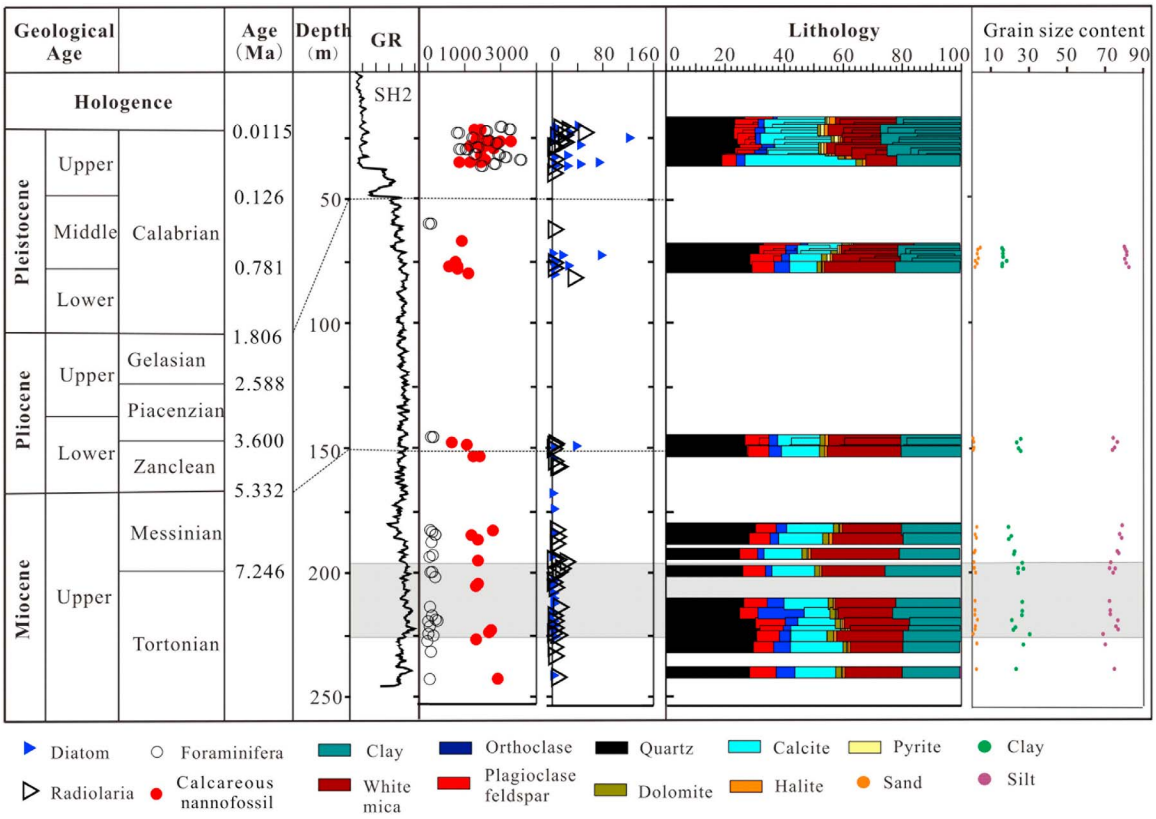

Figure 2. Drilling results for site SH2. Nannofossil information is after *Chen et al.* [2009]. Lithologic information is from *Lu et al.* [2009]. Grain size analyses are newly reported in this paper. Units are as follows: gamma ray; diatoms (number/g); radiolaria (number/5g); calcareous nannofossils (number/10view); foraminifera (number/g); and grain size (cumulative percent). The broken lines show the depths to Pleistocene/Pliocene (upper) and Pliocene/Miocene (lower) interfaces. The shaded zone shows the zone of gas hydrate–bearing sediments at sites SH2. The gamma ray log shows no sharp change in lithology at the depth of the hydrate-bearing sediments at site SH2.

(Figure 3). Of the few measurements made above 140 m, the chloride concentrations appear to decrease gradually from near-seawater values at the top of the core (563 Mm) to ~541 Mm near 145 mbsf. From 141 to 238 mbsf, the chloride concentrations drop sharply, ranging from 535 to 340 mM, with a minimal value of 312 mM at 204 mbsf. Gas hydrate saturation can be estimated based on the chloride anomalies [*Yuan et al.*, 1996] using

$$S_h = \frac{1}{\rho_h}\left(1 - \frac{Cl_{pw}}{Cl_{sw}}\right) \quad (1)$$

where $\rho_h = 0.924$ is the value of density of pure gas hydrate in g/cm^3 [*Sloan*, 1998]. Here, Cl_{sw} is the in situ baseline pore water chlorinity and Cl_{pw} is the measured chloride concentration in core water samples after gas hydrate dissociation [*Paull et al.*, 1996]. The chloride concentration of normal water was determined by smoothly fitting the chloride data above and below the gas hydrate zone with a second degree polynomial as the following:

$$Cl_{sw} = 0.0006z^2 - 0.3362z + 574.85 \quad (2)$$

where z is the depth in meters below seafloor. The baseline chloride concentration value is about 540 mM at site SH2. Using the chloride concentrations, gas hydrate saturation is estimated to be about 10 to 40% (Figure 4), with the maximum value 45% of the pore space at 205 mbsf (Figure 4).

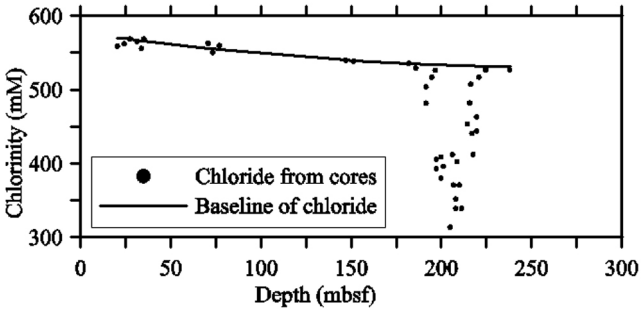

Figure 3. Measured chloride values (dots) from cores taken at drill hole SH2, and the baseline chloride concentration of normal pore water fit with a second-degree polynomial (black line). Chloride concentrations decrease sharply compared with the baseline chloride at depths where gas hydrate occurs (190–221 mbsf).The minimum measured value is 312 mM. The measured chloride values are also presented and discussed by *Wu et al.* [2010].

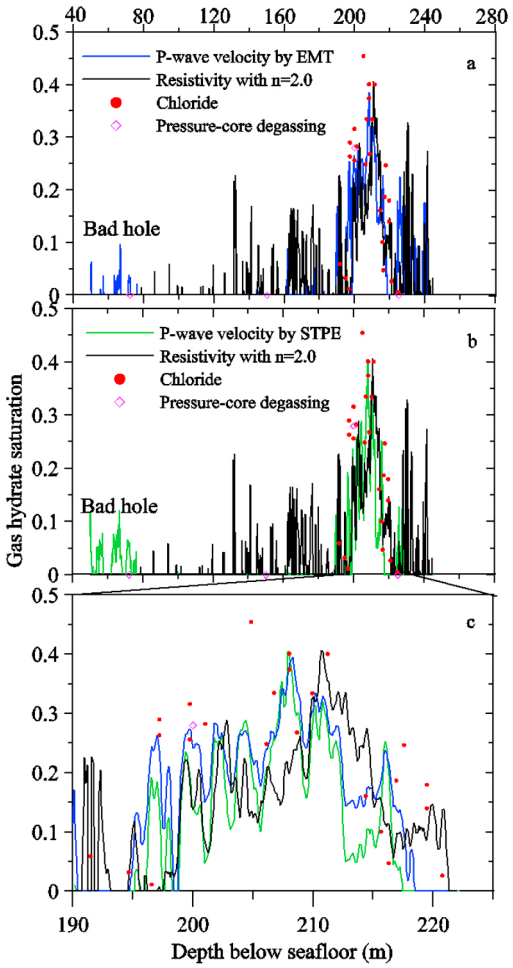

Figure 4. Gas hydrates saturations calculated from various methods at site SH2. (a) Gas hydrate saturation estimated using four estimates: from pressure core degassing (red diamonds); from chloride measurements (red dots); from resistivity with Archie values described in the text (black line); and from using effective medium theory (EMT) [*Helgerud et al.*, 1999] with parameters described in the text (blue line). (b) Same as Figure 4a, except that saturation estimated by the simplified three-phase equation (STPE) [*Lee*, 2008] is shown (green line) rather than the saturation estimated from EMT. (c) Enlargement of the interval 190–221 mbsf showing all five methods of estimating gas hydrate saturations.

4.1.2. Saturation From Resistivity

4.1.2.1. Porosity Calculations

[12] Sediment porosities must be known to estimate gas hydrate saturations using electrical resistivity. Porosity can be determined from analyses of recovered cores or from numerous borehole log measurements, such as from gamma density, electrical resistivity, neutron and velocity logs. Core-derived physical property data including porosities are often used to calibrate and evaluate the log-derived porosities. During expedition GMGS-1, water content, wet bulk density, dry bulk density and grain density were determined from recovered sediments. The core-derived porosities decrease from about 70% near the top of the hole (about 20 mbsf) to about 50% at depths of the gas hydrate–bearing sediments, although some layers have porosities nearer 40%.

[13] The bulk densities at site SH2 are highly variable due to poor hole conditions and range from a maximum of about 2.1 g/cm^3 to a minimum value of about 1.6 g/cm^3 (Figure 5). The lower values of density in some interval were probably caused by the enlarged borehole diameters (Figure 5, blue triangles). In general, *P* wave velocity and density have a linear relationship. The presence of gas hydrate sediments will increase the velocity and decrease the density slightly causing the crossplot points of velocities and densities to be more scattered (Figure 5, red circles). Because the borehole diameters are larger and density values are lower, without any apparent increases of resistivity and *P* wave velocity, these data are considered to be the result of bad borehole conditions and are therefore unreliable. We have removed them before using the log-derived bulk density (Figure 6c) to calculate porosity with the following equation:

$$\phi = \frac{\rho_g - \rho_b}{\rho_g - \rho_w} \tag{3}$$

where ρ_b is the bulk density from the well log, ρ_w is water density, and we use a constant equal to 1.03 g/cc and a grain or matrix density ρ_g equal to 2.65 g/cm^3. The density log yields erroneous high values for the borehole size below a diameter 20 cm at depths of 0 to 40 mbsf. The density porosities at site SH2 were therefore only calculated from 50 mbsf. The density porosity calculations from SH2 yielded values ranging from about 50% to 38% and higher values of about 55% in gas hydrate–bearing zone (Figure 6b).

[14] In general, the core-derived porosities have higher values than those calculated from bulk densities. Core-derived porosities are sometimes higher than log-derived

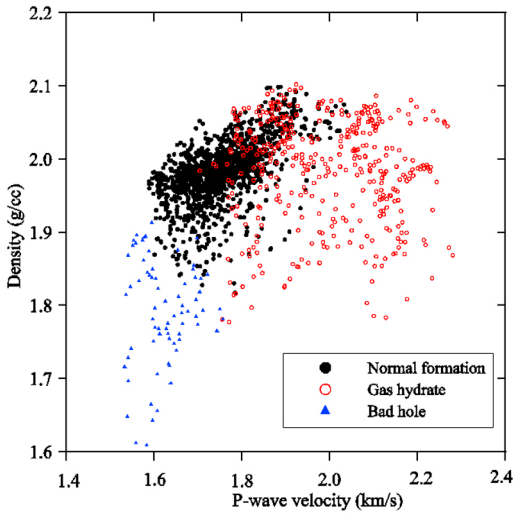

Figure 5. Crossplot between *P* wave velocity and gamma density. Black dots indicate the water-saturated density and *P* wave velocity at site SH2. Red circles are gamma density values at depths where gas hydrate–bearing sediment occurs (190–230 mbsf). Blue triangles are gamma density and *P* wave velocity values at the shallowest depths of drilling where bad borehole conditions are inferred.

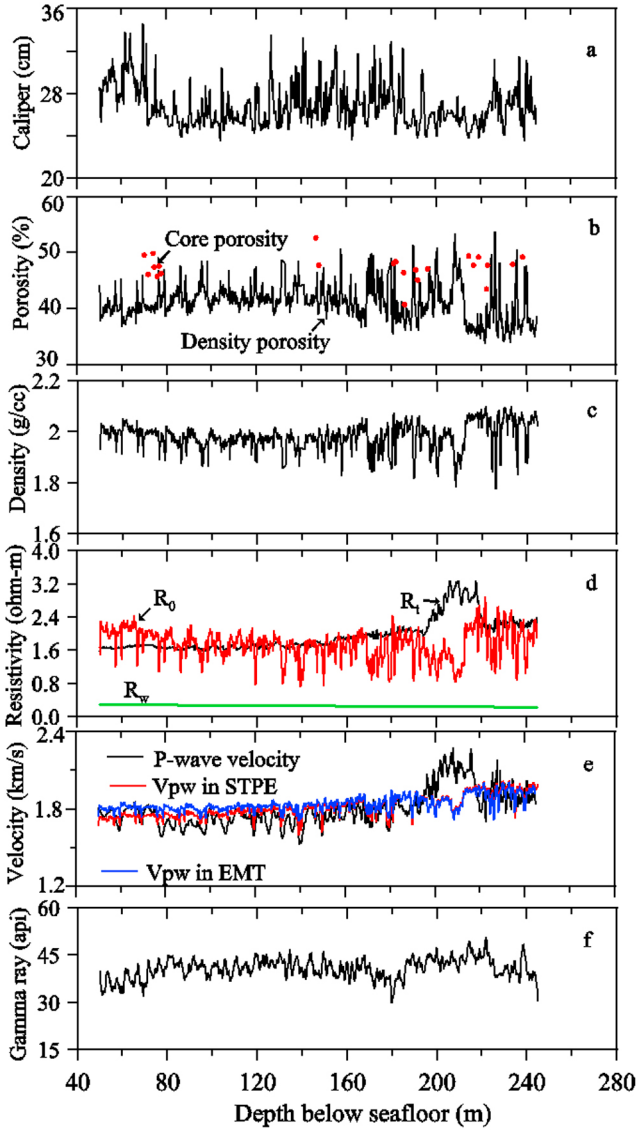

Figure 6. Wireline logs and analysis at site SH2. (a) The caliper correction hole SH2 indicating variations in hole diameter; (b) porosity calculated from the density log before removing the anomalously low values caused by poor borehole diameters (black line) and porosity measured in core samples (red dots); (c) gamma density from wireline log, anomalously low density values caused by the poor borehole diameter were removed; (d) resistivity of connate water calculated from the seafloor temperature, thermal gradient and salinity at site SH2 (green line), the measured resistivity (R_t, black line), and formation resisitivity of water-saturated sediments (R_0, red line); (e) compressional velocity (V_p, black line) and water-saturated velocity calculated by STPE (red line) and EMT (blue line) using values described in the text; (f) gamma ray log indicating the relatively homogeneous lithology at site SH2.

porosities because of mechanical and hydraulic rebound [*Hamilton*, 1976], though the expected difference at these depths would only be in the range of 4–5% at the depth of 300 m below seafloor in terrigenous sediments according to the empirical formula of *Hamilton* [1976], or much less than the differences shown in Figure 6b. This result suggests that the log-derived porosities may have significant uncertainty.

4.1.2.2. Water-Saturated Resistivity

[15] The formation of gas hydrate changes the physical properties of the sediment. The most readily observable change is an increase in resistivity, which is proportional to gas hydrate concentration [*Pearson et al.*, 1983]. If we assume that the resistivity anomalies are caused by the presence of gas hydrate in the sediments, in which the pore space is filled with water and gas hydrate, then the gas hydrate saturation S_h is given by *Archie*'s [1942] equation:

$$S_h = 1 - S_w = 1 - \left(\frac{R_0}{R_t}\right)^{\frac{1}{n}} \tag{4}$$

where S_w is water saturation, R_0 is the resistivity of the water-saturated sediment, R_t the measured formation resistivity and n an empirical constant. The resistivity of R_0 can be expressed using the equation as follows:

$$R_0 = \frac{aR_w}{\phi^m} \tag{5}$$

where R_w is the resistivity of the connate water, a and m are Archie constants, and ϕ is the porosity. The parameter m is commonly called the cementation factor and can be estimated from the formation factor (FF), defined as $FF = R_o/R_w = a\phi^{-m}$. If we use the formation factor in water-saturated sediments, the Archie parameters a and m can be estimated from a crossplot between porosity and formation factor. There are many different ways to interpret the crossplot because the data have large scatter (bad quality). In general, a is close to 1 and m is close to 2. The gas hydrate–bearing sediments from core samples occur in depths of 190–221 m (red points in Figure 7), Archie parameters a = 1.3 and m = 2.0 are estimated from the best fit curve to water-saturated sediments below the depth of 150 m (black squares, Figure 7). A group of data (blue triangles, Figure 7) shows large scatter, probably caused by the large scatter of density porosity for these data points. The baseline resistivity using the water-saturated values is shown in Figure 7 (purple line) and the R^2 value is about 0.344.

[16] The resistivity of connate water can be calculated using *Arp*'s [1953] formula if the salinity and temperature of formation water are known. Figure 8 shows the measured temperature in the borehole with a least squares fit (LSF) curve to the measured temperature. The LSF curve is given by T = 0.0456d + 5.6723, where T is the temperature in centigrade and d the depth in meters. The salinity of pore water was about 31 ppt. Figure 6d shows the calculated R_w as a green line. The resistivity of water-saturated sediments can be calculated by R_w, a, m and density porosity using equation (5). Figure 6d shows the measured resistivity (R_t) and water-saturated resistivity (R_0) at site SH 2.

4.1.3. Hydrate Saturations From Resistivity

[17] Gas hydrate saturation can be estimated from the resistivity log by equation (4) with a = 1.3, m = 2.0 and n = 2.0, which is shown in Figure 4 as a black line. At depths less than 120 m, the resistivity is generally less than that estimated for the water-saturated sediments (Figure 6d). For these depths, the gas hydrate saturations are estimated at

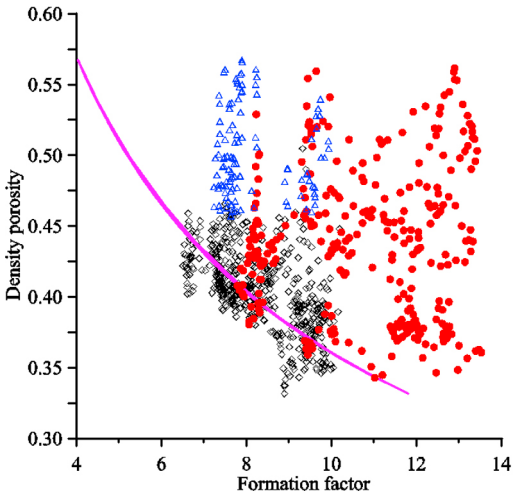

Figure 7. Relation between density porosity and formation factor for sediment samples below the depth of 150 m at site SH2. Red points refer to the samples of gas hydrate–bearing layer; triangles refer to samples caused by higher density porosity; black squares are water-saturated samples. Only the water-saturated samples are used to estimate resistivity and Archie parameters (purple curve). The Archie constant a = 1.3, m = 2.0 is appropriate for water-saturated sediments, and the R^2 value is about 0.344.

5–10% of the pore space. In the zone 190–221 mbsf, the resistivity is much greater than that of the water-saturated sediments and gas hydrate saturations reach a maximum of 40.5%, with an average value of 18% of the pore space (Table 1). At depths of 120–190 mbsf and at depths greater than ~221 mbsf, the resistivity is similar to or slightly higher than that of the water-saturated sediments (Figure 6d), yielding gas hydrate saturations of 10 to 30% of the pore space.

4.2. Gas Hydrate Saturations From Velocity

[18] The measured *P* wave velocity from wireline logging can also be used to estimate gas hydrate saturation by estimating first the portion of the velocity contributed by water-saturated sediment and then assuming that any additional positive velocity anomaly is caused by the occurrence of gas hydrate. We use two velocity models to estimate the velocity of water saturated sediment: the simplified three-phase equation (STPE) proposed by *Lee and Waite* [2008] and effective medium modeling (EMT) proposed by *Helgerud et al.* [1999].

[19] Both of these models use sediment composition, porosity, and the pore-filling material (water) to determine the velocity of water-saturated sediment, but each model treats the effect of gas hydrate on the physical properties slightly differently. Porosity input uses density porosity from wireline logging (Figure 6b). We assume that the sediment's solid phase includes five mineral components: quartz, feldspar, mica, calcite and clay. The mineralogy used in this study consists of 28% quartz, 12% feldspar, 26% mica, 14% calcite and 20% clay [*Lu et al.*, 2009]. In Table 2, we list bulk moduli (K), shear moduli (G), and density (ρ) for the materials used in the study.

4.2.1. Effective Medium Model

[20] The Effective Medium Theory (EMT) assumes that hydrate becomes a component of the solid phase, reducing porosity, cementing the dry sediment frame, and affecting the bulk and shear moduli [*Helgerud et al.*, 1999]. Essentially, this model allows hydrate to substitute for pore space as if the sediment were compacted (i.e., with a reduced porosity). The water-saturated bulk and shear moduli are calculated using the *Gassmann* [1951] equation. The bulk and shear moduli of the dry frame of sediments without gas hydrate can be calculated from the modified Hashin-Shtrikman-Hertz-Mindlin theory [*Dvorkin et al.*, 1999; *Ecker et al.*, 1998]. To estimate gas hydrate saturation, it is assumed gas hydrate is part of the dry sediment matrix and will reduce the porosity of the matrix. The effective elastic constants of the solid phase can be calculated from the mineral constituents in Table 2 and their moduli of each using *Hill*'s [1952] average. The critical porosity is equal to 0.36 and the average number of contacts is 8. The effective pressure (P) is calculated by the depth below seafloor (D), the acceleration due to gravity and sediment bulk density and water density by equation $P = (\rho_g - \rho_w)gD$.

[21] The water-saturated velocities using the EMT are shown in Figure 6e (blue line) and can be compared with the wireline velocities (black line). The interval in which the observed (wireline) velocities significantly exceed the water-saturated velocities is ~195–215 mbsf. Figure 4a (blue line) shows the gas hydrate saturations computed from the EMT model. In general, the saturations are less than 10% using this method except for the interval near 190–230 mbsf.

4.2.2. Simplified Three-Phase Equation Model

[22] The simplified three-phase equation (STPE) model differs from the EMT model in that the hydrate component is assumed to reduce porosity, but is not as effective in reducing porosity as non gas hydrate–bearing compacted sediment would be, i.e., a correction, ε, is applied to account for the reduced impact of hydrate formation relative to compaction, which increases the sediments moduli by reducing the porosity and increasing intergranular contacts [*Lee and Waite*, 2008]. *Lee and Waite* [2008] recommended $\varepsilon = 0.12$ for the correction to be applied to gas hydrate–bearing sediments. The consolidation parameter α depends on the effective pressure and degree of consolidation. *Mindlin* [1949] showed that the bulk and shear moduli depend on the 1/3 power of the effective pressure. *Lee and Collett* [2009a]

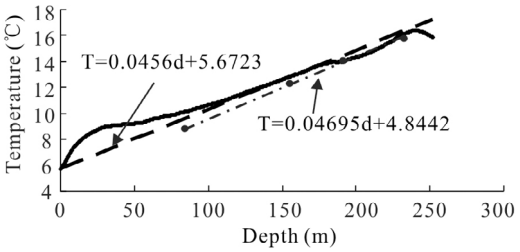

Figure 8. The wireline temperature log at site SH2 (black line) and the thermal gradient is 45.6°C/km calculated from measured temperature by a least squares linear fit curve (broken line). In situ temperatures were taken from Fugro Temperature Probe at four points (black points) producing the thermal gradient is 46.95°C/km.

Table 1. Gas Hydrate Saturations, S_h, Within the Downhole Log-Inferred Gas Hydrate Occurrences at Site SH2 on Shenhua Area, South China Sea

Methods	Depth of Gas Hydrate (mbsf)	Depth of Maximum S_h	Maximum S_h (%)	Average S_h (%)	Comparison of Variation Trends of S_h
Chloride	190–195	191.5	6.0	4.0	different
	196–215	206.0	45.0	29.3	same
	216–221	217.5	24.7	13.8	different
Resistivity	190–195	192.3	20.5	4.5	different
	196–215	210.7	40.5	18.0	same
	216–221	219.9	14.6	9.0	different
Velocity (EMT)	190–195	190.1	17.1	1.0	different
	196–215	208.1	38.5	22.1	same
	215–221	216	22.8	5.0	different
Velocity (STPE)	190–195	-	no	no	different
	196–215	207.8	41.0	18.0	same
	216–221	216	25.2	2.5	different
Pressure core degassing	78.0	-	0.0	-	-
	150.0	-	0.0	-	-
	197.5	197.5	27.08	-	-
	228.0	-	0.0	-	-

proposed the following equation for the depth (or effective pressure) dependence α:

$$\alpha_i = \alpha_0 (p_0/p_i)^n \approx \alpha_0 (d_0/d_i)^n \quad (6)$$

where α_0 is the consolidation parameter at the effective pressure p_0 or at the depth d_o and α_i is the consolidation parameter at the effective pressure p_i or at the depth d_i.

[23] The water-saturated velocity (Figure 6e, red line) was calculated by

$$\alpha_i = 45(100/d_i)^{0.71} \quad (7)$$

The water-saturated velocities using the STPE model are shown in Figure 6e (red line) and can be compared with the wireline velocities (black line). The interval in which the observed (wireline) velocities significantly exceed the water-saturated velocities is ~195–215 mbsf. Figure 4b (green line) shows the gas hydrate saturations computed from the STPE model. In general, the saturations are less than 10% using this method except for the interval near 190–230 mbsf.

4.2.3. Comparison of Results From STPE and EMT Models

[24] Figure 6e shows a comparison of the water-saturated velocities estimated using the EMT (blue line) and STPE (red line). Both lines follow identical trends although there are slight differences in the values (e.g., the estimated velocities from STPE are slightly lower in the depth of 60–160 mbsf). But the calculated water-saturated velocities are higher than the measured velocities at site SH2.

[25] Figure 4 compares the gas hydrate saturations based on the EMT (Figures 4a and 4c, blue line) and STPE (Figures 4b and 4c, green line). Gas hydrate saturation in the depth of 190–221 mbsf is enlarged and is shown in Figure 4c. The differences of gas hydrate saturations are shown in Table 1. The trends of gas hydrate saturation are similar at depths of 195–215 mbsf. The maximum gas hydrate saturations from the EMT and the STPE methods are 38.5% and 41.0%, respectively. The average saturation using the EMT is about 22.1% and the value using the STPE is 18.0%. Values from both methods are similar.

4.3. Gas Hydrate Saturations From Pressure Core Degassing

[26] Four successful pressure cores were recovered at full in situ pressure. Three cores were slowly depressurized and one core was rapidly depressurized to identify the gas hydrate. Methane mass balance analysis of the pressure core results showed that only one core (SH2–12R) at a depth of 197.5 mbsf was oversaturated in methane. The diameter of the Fugro pressure core is 51 mm; the sediment length was 69 cm measured from gamma density and X-ray. The sediment porosity was 39% calculated from density (Figure 6b), yielding a pore volume of 0.549 L. During depressurization, the core released 26.7 L of methane, or 1150.5 mmol. The methane saturation in this core is 113 mM, as calculated from *Xu* [2004] and *Xu et al.* [2001] using a water depth of 1238 m, a thermal gradient of 46.95°C/km, a seafloor temperature of 4.84°C, and an in situ salinity 30.0 ppt. The maximum dissolved methane in the pore fluids calculated from the pore volume and methane saturation is 62.04 mmol. The methane hydrate saturation is 27.08% of the pore volume assuming all gas hydrate is evenly distributed throughout the pore volume (Figure 4).

5. Distribution of Gas Hydrate From Seismic Data

5.1. BSR Identified From Seismic Profiles

[27] A regional BSR can be identified from 3-D seismic data (Figure 9) and high-resolution 2-D seismic profiles (Figures 10 and 11) that cross site SH2. SH2 is located on a

Table 2. Mineral Components and Elastic Moduli and Density of Minerals for Site SH2

Material	$K(GPa)$	$G(GPa)$	$\rho(g/cc)$
Calcite	77.0	32.00	2.71
Feldspar	76.0	26.0	2.71
Clay	20.9	6.85	2.58
Quartz	36.6	45.00	2.65
Mica	62.0	41.0	2.68
Methane hydrate (5 MPa, 273 K)	8.41	3.54	0.922
Methane gas (10 MPa, 273 K)	0.015	0	90
Quartz 28.0% + feldspar 12% + mica 26% + Clay 20.0% + Calcite 14.0%[a]	45.27	26.0	2.667

[a]See *Lu et al.* [2009] for core analysis (Figure 2).

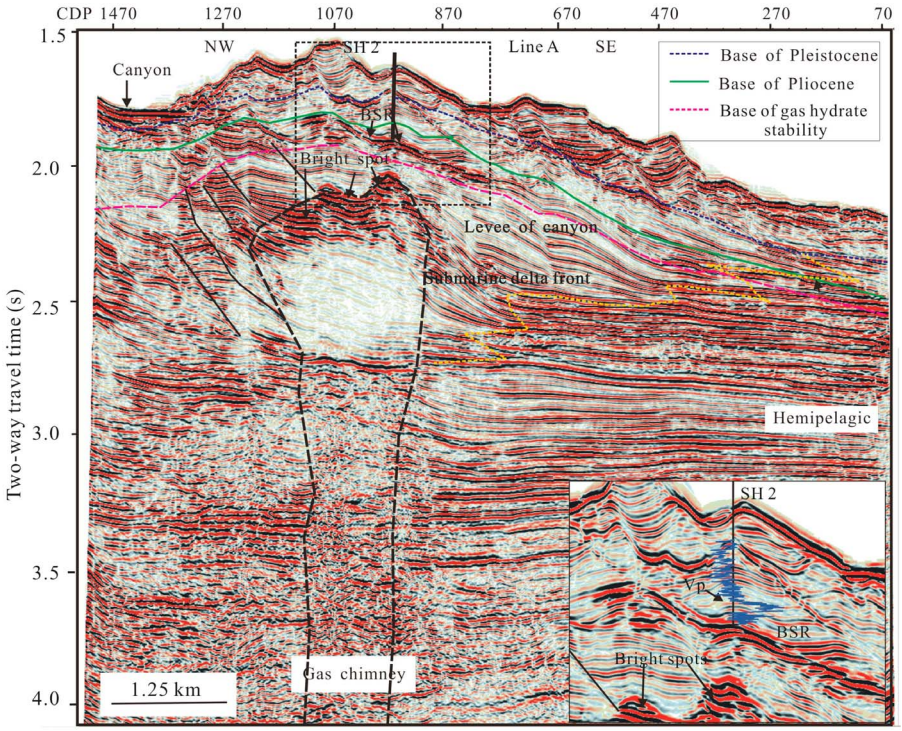

Figure 9. Interpretations of the 3-D seismic line A across site SH2. SH2 (vertical black line) is located in the levee of one of the canyons shown by *Zhu et al.* [2010] belonging to a submarine delta front (yellow dashed line). The gas chimney below the BSR is characterized by bright spots at its top and blurred reflections at 3–4 s within the chimney pipe. The blanked area is probably an amplitude artifact generated by the strong amplitudes at the top of the chimney. The insert shows details around site SH2, including *P* wave velocity (V_p) measured at the drill site.

ridge between two canyons. The BSR at the crest of ridge is nearly the brightest subseafloor reflection. This reflection has reversed polarity, roughly parallels the seafloor, and intersects dipping and deformed stratigraphic horizons. The inversion results (Figure 11) show that the compressional velocity is near ~1.4 km/s, which is less than the velocity of seawater, and occurs at depth associated with the BSR. These data are consistent with the presence of free gas causing the BSR. The well logs do not show a velocity anomaly at these depths near the base of the well, which may be because the amount of free gas is small, rendering the effect on the high-frequency velocity log insignificant [e.g., *Lee and Collett*, 2009b] in unconsolidated sediments or the well does not penetrate through the BSR.

[28] Acoustic responses like bright spots with low frequency and low velocity [*Xu et al.*, 2010; *N.Y. Wu et al.*, 2009] are shown below the BSR, similar to responses observed at locations where hydrocarbons occur. The vertical zones of deteriorated seismic data quality and reduced amplitudes are often referred to as gas chimneys [*Arntsen et al.*, 2007]. Some layering and reflections are preserved within the gas chimneys but are blurred or pulled down in the presence of free gas (Figure 11). The gas chimneys in Figures 9–11 do not reach the seafloor but terminate below the BSR.

5.2. Gas Hydrate Stability Zone (GHSZ)

[29] The thickness of the gas hydrate stability zone can be estimated two ways: using the depth of the BSR as the base of GHSZ (BGHSZ), or using the temperature-pressure-gas composition information to estimate the base of GHSZ [e.g., *Dickens and Quinby-Hunt*, 1994].

[30] In situ temperatures measured at five sites show that thermal gradients range from 45 to 67.7°C/km. Near site SH2, the thermal gradient in shallow sediments (<10 m) obtained from Jianyu-1 heat flow probe is about 68.7°C/km [*Li et al.*, 2010]. In situ temperatures were taken from the Fugro Temperature Probe located at different depths in the borehole (Figure 8), producing an estimated thermal gradient of 46.95°C/km. The wireline temperature log shows that temperature increases quickly from the seafloor to 30 m and then decreases slightly, which indicates that thermal gradient may be variable at different depths below the seafloor. The thermal gradient below depths of 100 m is about 45.6°C/km (Figure 8). The estimated depths of BGHSZ are ~270 m and ~259 m for thermal gradients of 45.6 and 46.95°C/km, respectively. These estimates are made assuming pure methane gas content, which is consistent with measurements of ~99.21% methane in subbottom depths between 150 and 228 m [*Wu et al.*, 2008, 2010]. The total depth of site SH2 is about 245 m, which is shallower than the BSR in seismic line A (Figure 9), indicating that the BGHSZ must be slightly deeper than 245 m.

5.3. Lateral Extent of Gas Hydrate

[31] Because well log data provide detailed information only at the well locations, the lateral extent of gas hydrate must be estimated from other methods. We have utilized

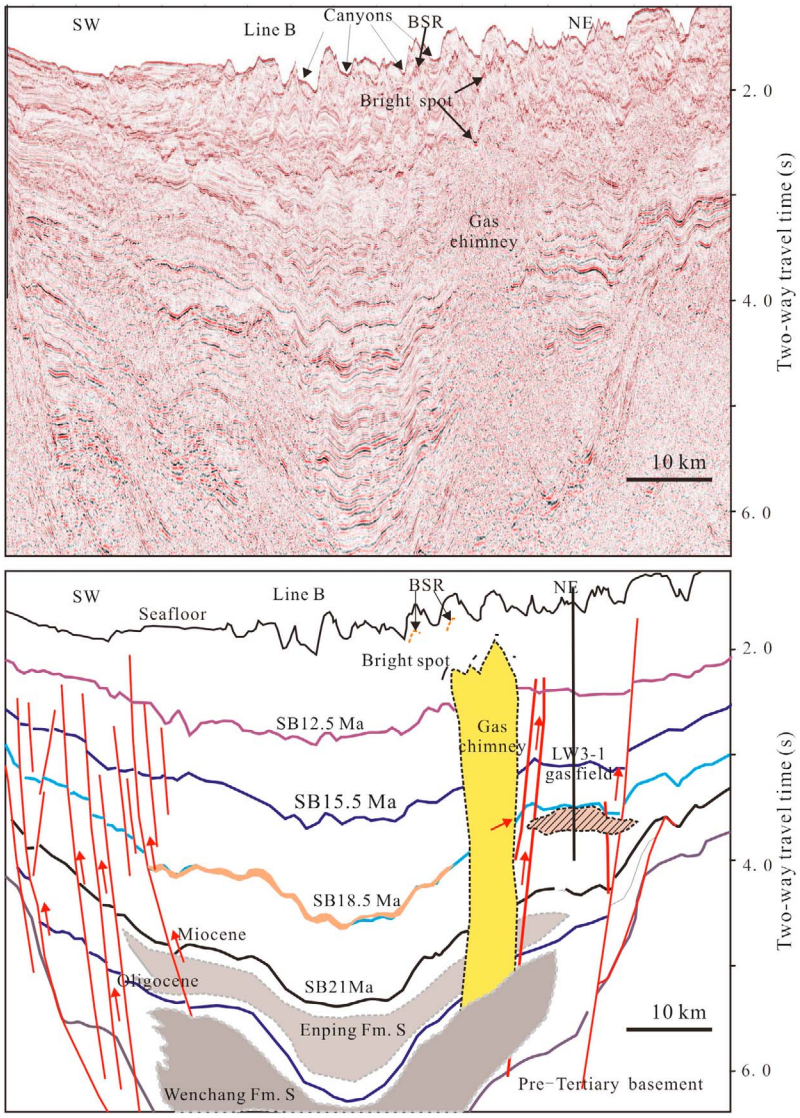

Figure 10. Regional seismic reflection profile B showing gas migration pathways (red faults and gas chimney) and possible gas source at depth (shaded areas). Location of the LW3–1 gas field and the BSR (yellow line) are also shown. The location of the section is shown in Figure 1b. SB, chronostratigraphic sequence boundary.

P wave velocity derived from seismic data by constrained sparse spike inversion (CSSI) to extend the well information along the seismic profile, similar to the approach used in a comparison of gas hydrate distribution in the Blake ridge and South China Sea [*Lu and McMechan*, 2002; *Wu et al.*, 2007; *Wang et al.*, 2006]. Seismic data are band limited; hence the CSSI acoustic impedance data can be used to obtain low-frequency and high-frequency information by merging the low-frequency trends in the impedance logs of wells [*Lindseth*, 1979]. The input includes the time-migrated seismic data, the seismic wavelet, the interpolated control horizons and the interpolated low-frequency impedance trend. Because the CSSI produces the acoustic impedance estimations rather than *P* wave velocities, the *P* wave velocities were derived using the relation between velocity and density proposed by *Gardner et al.* [1974] with revised parameters that reflect the physical properties of the local sediment. Figure 11a shows the seismic profile; SH3 and SH7 are located along this seismic profile and SH2 is ~500 m away from the profile.

[32] Figure 11b compares the seismic data with a synthetic seismogram using the *P* wave velocity calculated from acoustic impedance for SH2. The acoustic velocity for wireline data at SH2 are also shown in Figure 11b. The CSSI inversion closely mimics the wireline log, although it lacks the high-frequency variations inherent in the well log data. The inversion also shows a clear velocity increase at the inferred depths of the gas hydrate bearing sediment (190–220 mbsf).

[33] Figure 11c shows a higher compressional velocity layer with a value ranging from 1.8 to 2.3 km/s above the BSR, but it is discontinuous laterally and has different thicknesses. The velocity of gas hydrate–bearing layer is about 1.9 to 2.0 km/s at SH3 and it is about 2.0 to 2.1 km/s

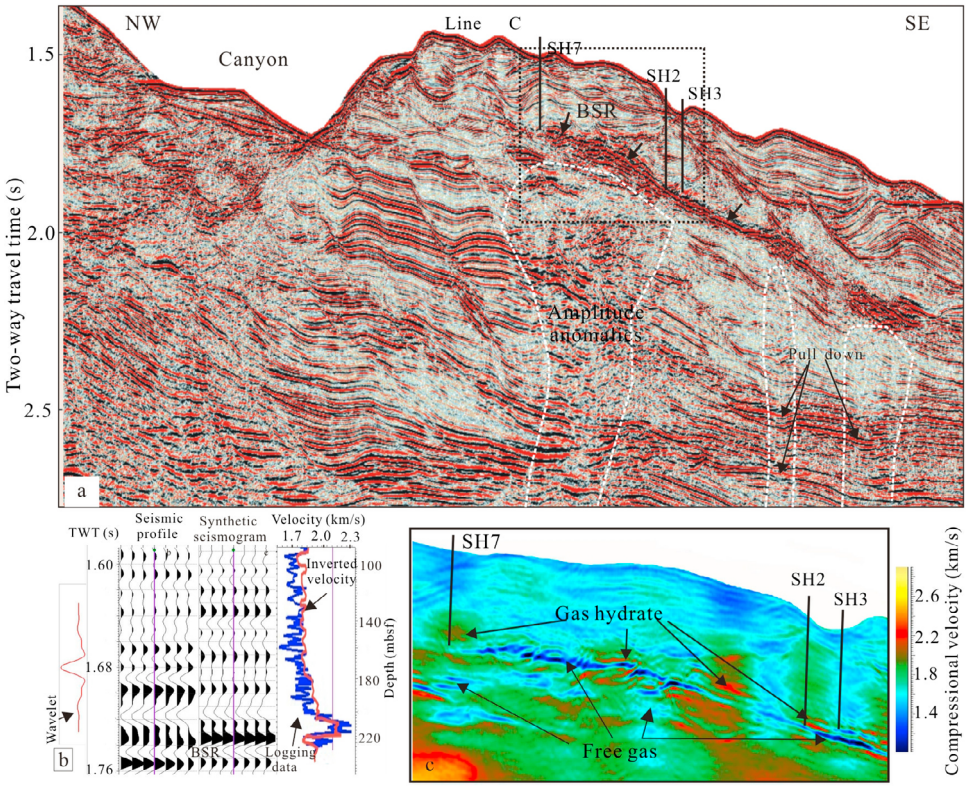

Figure 11. (a) Seismic line C along sites SH7, SH2, and SH3. Site SH2 is not located on this profile; its location is projected onto the seismic line. A very strong BSR occurs at the drilled sites. Gas chimneys (white dashed lines) are shown below the BSR with amplitude wipeout and reflection pull down, indicating the presence of free gas. (b) (left) Seismic traces at site SH2, (middle) synthetic seismogram traces using the wavelet shown at the extreme left, and (right) *P* wave velocity from wireling logging (blue line) and inverted *P* wave velocity from CSSI (red line); (c) *P* wave velocity profile from seismic line C. Higher velocities occur above the BSR and are interpreted to indicate the presence of gas hydrate; low velocities occur beneath the BSR and are interpreted to indicate the presence of free gas. Both the high- and low-velocity anomalies have patchy distributions.

at SH7. The velocity at SH2 is the highest of the three sites, which is about 2.0 to 2.2 km/s. The gas hydrate zone inferred by velocity inversion in Figure 11c is similar to that obtained from well log data, i.e., slightly above the BSR. These results suggest that the distribution of gas hydrate is spatially heterogeneous. Below BSR, the velocity inversion shows a low value of 1.3 to 1.6 km/s, indicating the presence free gas in this zone (Figure 11c). The acoustic velocity of the well log does not show any velocity anomaly at this depth, which implies that the amount of free gas in the sediments could be very small. The effects of small amounts of free gas on high-frequency well log may not be detectable [*Lee and Collett*, 2009b]. The low velocity is also in patchy distribution below the BSR.

6. Discussions

6.1. Comparison of Various Gas Hydrate Saturations

[34] We used five methods to estimate gas hydrate saturations and compared to saturation estimated from depressurization experiments [*Schultheiss et al.*, 2009] at site SH2, South China Sea (Figure 4): chlorinity from the pore waters of the core samples, resistivity using the Archie equation, and two estimates from velocity models (EMT and STPE). We use the velocity models of effective medium theory [*Helgerud et al.*, 1999] and simplified three-phase Biot-type equations [*Lee*, 2008] to estimate gas hydrate saturations because the velocity models were derived from considering the elastic properties of the unconsolidated porous sand reservoir. The estimated gas hydrate saturations are affected by the porosities, sediment components and their contents and the assumed constant parameters in the calculation method of bulk and shear moduli. The various methods have similar trends in saturation curves in the gas hydrate–bearing sediments, showing slightly different values in some intervals. The differences in maximum hydrate saturation (Table 1) range from 38.5% (EMT velocity) to 45.0% (from chloride) with the STPE velocity and resistivity estimates intermediate (41.0% and 40.5%, respectively). Maximum saturations occur in the same depth ranges, at 205 mbsf (from chloride) to 211 mbsf (resistivity). Average gas hydrate saturations estimated from chloride have the highest value of 29.3 at depths of 195–215 mbsf, and those estimated from resistivity and the STPE velocity model are about 18%. The average gas hydrate saturation estimated from EMT velocity is about 22.1% (Table 1 and Figure 4). Neither the STPE nor EMT methods

show gas hydrate saturations at depths shallower than 190 mbsf except at depths of 50–70 mbsf where bad borehole conditions render the results unreliable. Few cores were collected above 190 mbsf for estimating gas hydrate saturations from chloride. Overall, the gas hydrate saturations calculated by the four methods have remarkably consistent and similar trends at depths of 190–221 mbsf, which have similar saturations from pressure cores degassing at the depth of 197.5 mbsf in Figure 4 (diamond) [*Schultheiss et al.*, 2009].

[35] A number of reasons can explain these small saturation differences. The calculations assume the sediments are isotropic for both velocity and resistivity estimates, although the lithologies are clearly variable and heterogeneous (clayey silt and clay). Hence, the parameters are optimum for some depths and inaccurate for other depths. This will cause differences in the estimates. Porosity is another parameter that affects the calculated gas hydrate saturations. We have eliminated presumed bad measurements by evaluating the crossplot between density and velocity (Figure 5), which is used to calculate density porosity, and the calliper of the borehole, where large hole size indicates bad coupling and unreliable measurements. Small changes in parameters used in the Archie equation (resistivity method) will affect estimates of gas hydrate saturation. In situ temperature is required to calculate the resistivity of connate water and R_w affects the estimation of Archie parameters a and m. We used the wireline temperature log, which results from a mix of temperatures of the borehole fluid circulation and an interaction with the formation. However, in estimating gas hydrate saturations, the apparent resistivity ($R_a = aR_w$) rather than R_w is used. Therefore, even if there is some error in R_w caused by temperature, the gas hydrate saturations estimated from the resistivity is not significantly affected as long as the calculated baseline resistivity follows the measurement reasonably well. The Archie parameters are determined by the crossplot between the formation factor and density porosity (Figure 7). The crossplot does not show a clear relation due to poor data quality. There are many different ways to interpret the crossplot that will give different values of the Archie constants. We used a = 1.3, m = 2.0 and n = 2.0 to estimate gas hydrate saturations for isotropic resistivity analysis based on the relations for depths below 150 mbsf which is where gas hydrate occurs.

[36] In the velocity models, the water-saturated velocities are calculated by assuming that the porosity contains water. The estimated gas hydrate saturations depend on accurate estimates of porosities. In the shallowest part of the core, above about 50 m, the gas hydrate saturations are influenced by the poor density log and poor density porosity log attributed to bad borehole conditions (expanded caliper values, Figure 6a). Hence saturations calculated at these shallow depths are not considered reliable. Additional bad borehole conditions may exist at other depths (e.g., ~130–180 mbsf) where the diameters of the borehole change greatly (Figure 6a).

[37] Uncertainties in the calculated gas hydrate saturations from downhole measurements come from two different sources: (1) errors associated with uncertainties in downhole measurements and (2) errors associated with uncertainties in parameters selected for the equations [*Lee and Collett*, 2001]. Porosity is a measurement error associated with uncertainties in the acoustic method and the resistivity method. For the EMT method, error is associated with the selection of effective pressure, the critical porosity and the average number of contacts per grain in a sphere packs at critical porosity. For the STPE method, there are two free parameters, α and ε to be determined in calculating gas hydrate saturation [*Lee and Waite*, 2008]. For the resistivity method, error is associated with the selection of Archie's constants, a and m, as well as the resistivity of connate water (R_w). Figure 6b shows that the difference between density porosity and core porosity is about 7%, which is larger than the empirical formula derived for these properties in deep-sea sediment [*Hamilton*, 1976]. The log-derived density porosity may therefore contribute significant uncertainty to estimates of gas hydrate saturation. Gas hydrate saturation errors (ΔS_h) associated with the porosity error ($\Delta\phi$) and Archie parameter a are given by *Lee and Collett* [2001]:

$$\Delta S_h = \frac{m(1 - S_h)}{n} \frac{\Delta\phi}{\phi} \tag{8}$$

$$\Delta S_h = \frac{-(1 - S_h)}{n} \frac{\Delta a}{a} \tag{9}$$

[38] Applying these equations shows that an observed average value of 7% difference between core and density porosity will yield an estimation error of about 7% at zero gas hydrate saturation and about 4% at 40% saturation. The crossplot used to estimate density porosity (Figure 7) does not show a clear relation between the formation factor and density porosity due to poor data quality. The data below the depth of 150 mbsf (Miocene) were used to calculate Archie parameters by moving the anomalies caused by higher porosity, which may be unfit for the whole wireline logging. The estimation error for the low gas hydrate saturations (i.e., less than 7% or conservatively 10%) will be larger than that for high gas hydrate saturation [*Lee and Collett*, 2001]. Therefore, the low gas hydrate saturations (<10%) are probably explained by the estimation errors from wireline logging measurements or the input parameters in calculating saturation and are considered below the detection levels of our methodologies.

6.2. Gas Hydrate Petroleum System Near Drill Site SH2

[39] In a gas hydrate petroleum system, the individual factors of the following are favorable for the formation of gas hydrate occurrences in the sediments [*Collett et al.*, 2009]: (1) appropriate gas hydrates stability conditions; (2) presence of a gas source; (3) availability of water; (4) indicators for the migration of gas; (5) occurrence of reservoir rocks, traps, and seals; and (6) timing. At site SH2, the gas is primarily methane (with a value of 99.6%). The salinity and thermal gradient are 30 ppt and 45.6°C/km, respectively. The thickness of the gas hydrate stability is about 270 m. Gas hydrate in Shenhu area is distributed in relatively homogenous sediments and occurs above the base of gas hydrate stability. There may be higher saturations in thin coarse-grained layers, but the sediment components were only analyzed every 100 cm which show that the sediments mainly consist of silt (Figure 2). Silt covers a large

grain size range from 4 to 62 microns, which may make the higher-saturation gas hydrate layer seem homogeneous and indistinguishable from the deeper and shallower sediments when it might actually be different by having coarser silt sizes. Unfortunately, the data do not differentiate within the silt category, so it is not possible to know whether there are variations of finer and coarser silts. The variations within the silt size category could affect the nature of the sediments and their ability to host gas hydrate, such as reported in the test well of Mount Elbert, Alaska northern slope [*Winters et al.*, 2010]. The factors such as gas source, gas migration, and reservoir appear to control the formation of gas hydrate at site SH2. An increase in the abundance of relatively large calcareous fossils and foraminifer in fine-grained sediments may increase the size of pore spaces and decrease the capillary force between grains. Increased pore space associated with broken foraminifera should provide nucleation sites for gas hydrate. The decreased capillary force may enhance gas hydrate formation by enhancing gas flux into the GHSZ. This occurs when the buoyancy pressure at the top of the gas chimney exceeds the capillary entry pressure at the base of GHSZ, allowing gas to move into the GHSZ, forming more gas hydrate.

6.2.1. Gas Source at Site SH2

[40] Microbial generation of methane generally occurs in most continental margin sediments around the world and probably contributes to a biogenic methane component at site SH2 [*Wu et al.*, 2010]. Establishing average gas hydrate saturations of 20% and maximum saturations up to ~45% (such as found at site SH2) by in situ microbial methane alone is difficult [e.g., *Xu and Ruppel*, 1999], hence a method for concentrating gas hydrate, for example, through enhanced gas flux, could explain our observations. On the other hand, *Malinverno* [2010] applied a mass balance model to gas hydrate formation in thin sand only considering the in situ microbial conversion of a small amount of organic carbon at site U1325 off western Canada and interpreted the vertical distribution and gas hydrate saturation with maximum values of 20–60% of pore space at this site can be explained by in situ microbial methane generation.

[41] A thermogenic component of methane may also be present based on recent geochemical analyses of gas composition and carbon isotopes, headspace gas and sediment samples from gas hydrate drilling area [*Huang et al.*, 2010]. Methane to ethane ratios (C_1/C_2 values) are higher than 1205 between the seafloor and 190 mbsf and decrease to 575–736 at depths below 190 mbsf [*Wu et al.*, 2010]. The C1/C2 value of the core SH2–12R recovered within the hydrate-bearing sediments ranges from 330 to 428. Carbon isotopic analyses from gas hydrate samples recovered from sites SH2, SH3, and SH5 show that $\delta^{13}C_1$ values range from −54.1 to −62.2‰ and δD_{CH4} values vary from −180 to −255‰ at the drilling zone. $\delta^{13}C_1$ and δD_{CH_4} $\delta^{13}C_1$ and δD_{CH4} values from core SH2–12R are −56.7‰ and −199‰, respectively [*Huang et al.*, 2010]. Acid digestion analyses of 113 sediment samples in the drilling sites of SH1, SH2, SH5 and SH7 indicated that methane concentration is mostly higher than 90%. The values of $C_1/(C_2 + C_3)$ ratio are lower than 50 and $\delta^{13}C_1$ values range from −29.8 to −48.2‰. Gas hydrate drilled at site SH2 is near to the LW3–1 (Figure 1a). The pay formations of LW3–1 gas field are marine sandstones of the Oligocene Zhuhai and lower Miocene Zhujiang formations and the reservoir rocks overlay the coal-bearing strata of the Enping formation (Figure 10). The total organic carbon (TOC) content of these deeper thermogenic source rocks is significant. In the deeper Eocene source rocks, such as the Wenchang Formation in the basin, the shale has TOC values ranging between 0.65 and 5.22%. In the Oligocene source rocks, such as Enping Formation, the shale has a TOC values ranging from 0.3 to 5.6%. The gases are composed predominantly of hydrocarbon gas (>96%) [*Zhu et al.*, 2009]. Thermal history modeling of the LW 3–1 well 21 km away in the Shenhua area indicates that the Oligocene Enping Formation is currently mature to highly mature and the Eocene Wenchang Formation is overmature [*Zhu et al.*, 2009]. These units are deeper than the zone where gas hydrate is inferred to occur at site SH2. The main gas source entered its peak gas generation window during the late Miocene and Pliocene and may be associated with bright spots identified below the GHSZ at site SH2 [*Huang et al.*, 2003].

6.2.2. Gas Migration

[42] Methane, along with other hydrate-forming gases, migrates within a sedimentary section by three processes: (1) diffusion, (2) fluid flux (e.g., as a gas dissolved within migrating water), or (3) as bubbles [*Collett et al.*, 2009]. Migration of gas by diffusion is a very slow process and generally cannot form high-saturation gas hydrate accumulations [*Xu and Ruppel*, 1999]. Methane flux by advection, either as a dissolved gas or as a separate gas bubble phase, is probably the dominant processes forming higher gas hydrate saturations at site SH2.

[43] Faults and gas chimneys are shown clearly in seismic data below the GHSZ (Figures 9, 10, and 11), which can create pathways for fluid vertical migration. Moreover, sandstones deposited on the unconformities have been shown to be the preferred conduits for lateral gas migration in the deep water area [*Pang et al.*, 2006]. The seismic anomalies (bright spots and gas chimneys) caused by hydrocarbon leakage [*Meldahl et al.*, 2001; *Deptuck et al.*, 2003; *Hansen et al.*, 2005; *Mayall et al.*, 2006; *Gay et al.*, 2007; *Cartwright et al.*, 2007; *Løseth et al.*, 2009] have been identified below GHSZ. Because of the high gas hydrate saturations, we propose that the advective upward migration of methane from deeper sediments is a source of gas for the formation of higher gas hydrate saturation at site SH2.

[44] A proxy for methane flux near the seafloor is often associated with the depth to the sulphate-methane interface [*Paull et al.*, 1996; *Wu et al.*, 2008]. The sulphate-methane interface (SMI) at site SH2 is about 26 m, deeper than could be obtained from gravity and piston coring. In nearby sites, the SMIs of SH3 and SH7 are 27 m and 17 m, respectively, which imply that the vertical flux of methane is relatively low in each of the drill sites [*Wu et al.*, 2008, 2010]. These SMI depths are shallower than those at some passive margins (e.g., the Blake Ridge, at 60 m depth [*Paull et al.*, 1996]), but considerably deeper than sites with presumed large vertical fluxes (such as the Gulf of Mexico [*Paull et al.*, 2005]), and provide a mechanism for moving and concentrating methane into the gas hydrate stability zone.

[45] Site SH2 exists in a region of submarine canyons that have been migrating northeastward as a result of the interplay of gravity flows and bottom currents in PRM basin

from the middle Miocene to present, with the modern canyons being 30–60 km long, 1–5.7 km wide, and from 50 to 300 m tall in water depths of 450–1500 m. [*Zhu et al.*, 2010]. Stratigraphic successions are characterized by basal erosional discontinuities at the canyons' bases and subsequently partially filled by canyon thalweg deposits. Due to the high porosity of silt and sand of the canyons infills, the thermogenic fluids migrating from underlying source rocks can be concentrated in these coarser units. The canyons are acting as effective longitudinal drains for fluids to selectively migrate along fault and chimneys [*Gay et al.*, 2006]. SH2 was drilled on a ridge between two canyons. The thermal geometry of ridges and adjacent canyons causes fluids (containing methane) to migrate from the deeper sediments and be trapped at crests of the ridges [*Ruppel*, 2001; *Nimblett and Ruppel*, 2003]. This provides another mechanism for methane to move into the gas hydrate stability zone at site SH2.

6.2.3. Gas Hydrate Reservoir

[46] The gas hydrate saturation with maxima up to 38.5–45% (Table 1) at site SH2 is uncommon in silt and clay dominated sediments. Most mean saturations of gas hydrate in fine-grained sediments are low, similar to the results from the Blake Outer Ridge [*Paull et al.*, 1996]. In general, higher-saturation gas hydrates are found in coarse-grained or fractured sediments. In the northern Cascadia margin, gas hydrate occupies up to 60% of the pore space in the coarse-grained horizons at site U1325 and >80% at site U1326 [e.g., *Torres et al.*, 2008; *Malinverno et al.*, 2008]. In the Gulf of Mexico at KC 151, gas hydrate saturation is greater than 20% of the pore space in fractured sediments [*Ruppel et al.*, 2008]. Higher gas hydrate saturation can be explained by the sand content of the sediments if sufficient methane is present.

[47] Gas hydrate is interpreted to be distributed throughout the interval of 190–221 m at site SH2. It occurs in a homogeneous layer just above the base of the GHSZ [*Schultheiss et al.*, 2009]. Site SH2 has a peculiar mineral content of the sediments owing to the abundance of calcareous fossils (in general 4–10 μm) and foraminifer (mostly >0.063 mm), which have larger particle than the clay sediments [*Chen et al.*, 2009]. In most fine-grained sediments, the menisci of interfacial water have extremely small radii [*Klausner*, 1991], which results in strong capillary forces, which tend to inhibit the formation of gas hydrate. At site SH2, the mineral components and their contents change slightly in the gas hydrate–bearing layer. There is no sediment components analysis at the depth of the maximum of saturation computed from chlorinity because the core samples were only analyzed every 100 cm (Figure 2), thus it is difficult to interpret whether the maximum saturation is associated with a thin sand layer below the resolution of our measurements or with another geological feature. An increase in the abundance of radiolarite (calcareous fossils) and foraminifer was indicated, which can increase the size and roundness of pore spaces in the fine-grained sediments and decrease the capillary forces of grains (Figure 2). Moreover, the shells of foraminifer were clear and partly broken, which can supply more effective space for the formation of gas hydrate. The presence and size of foraminifera not only enhance the permeability of the sediments but also provide nucleation sites for the formation of gas hydrate [*Chen et al.*, 2010] similar to the situation in Blake Ridge [*Kraemer et al.*, 2000].

6.3. Model for Occurrence of Gas Hydrate in Site SH2

[48] In the fine-grained sediments of the Shenhu area, South China Sea, gas hydrate saturations with a maximum value of 45% in the pore space occur at the depth of 190–221 mbsf, above the base of the gas hydrate stability zone. Low gas hydrate saturations in the shallower sediments may be below the level of detection using our methodologies. The occurrence of gas hydrate in this area (Figure 12) can be explained by two of the models reviewed by *Collett et al.* [2009]. In the first model (Figure 12a), the low-saturation gas hydrate is formed mostly with low fluid flow in fine-grained sediments. Methane concentrations in the fluids may not be sufficient to exceed maximum saturation at the top and bottom of the stability zone, with gas hydrate forming only where the methane concentrations (red line) exceed solubilities (green line). This causes a limited, low-saturation (and possibly undetected and undetectable) accumulation of gas hydrate in the hydrate stability zone [*Xu and Ruppel*, 1999; *Collett et al.*, 2009].

[49] The second model involves a mechanism for concentrating gas hydrate near the base of the stability zone, as observed at site SH2 (Figure 12b). In this model, an increase in fluid flux and/or in methane concentrations causes the zone of hydrate occurrence to grow (the area between the red (methane concentration) and green (methane solubility) lines, similar to the model proposed by *Ruppel and Kinoshita* [2000]. One mechanism for increasing the methane flux and concentration was proposed by *Liu and Flemings* [2007] in silt environments where water flux is minimal. A gas column may develop below the regional hydrate stability zone in which gas is stored below the base of the GHSZ. When the buoyancy pressure exceeds the capillary entry pressure, gas flows into the gas hydrate–bearing zone allowing gas hydrate to form above the BSR [*Liu and Flemings*, 2007]. The migration of gas into and through gas chimney like mud volcanoes may be episodic and difficult to observe [*Løseth et al.*, 2009]. This migrating gas from the deeper sediment could be either biogenic or thermogenic and becomes the source of gas hydrate in the higher-porosity sediments near the base of the gas hydrate stability at site SH2 causing the observed higher saturations (Figure 12b).

[50] Another mechanism for concentrating gas hydrate is through the continued deposition of sediment causing the base of the GHSZ to migrate to a shallower depth [e.g., *Paull et al.*, 1996]. This upward shift causes the dissociation of the deepest gas hydrate, releasing methane to migrate upward back into the GHSZ which, over geologic time, increases gas hydrate saturations near the base of the GHSZ. At site SH2, canyon migration resulting in accretion on the intracanyon ridges [*Zhu et al.*, 2010] may enhance this process.

7. Conclusions

[51] Gas hydrate saturations were estimated using five methods: core-derived chloride anomalies, downhole electrical resistivity logs, pressure core degassing, velocity using effective medium theory [*Helgerud et al.*, 1999] and velocity using simplified three-phase equation [*Lee*, 2008]. The highest gas hydrate saturations are located at depths of ~190–221 mbsf, above the BSR, and consist of average saturations of ~20% and maximum saturations of 38.5–45%. The higher gas hydrate saturations, calculated from resistivity and

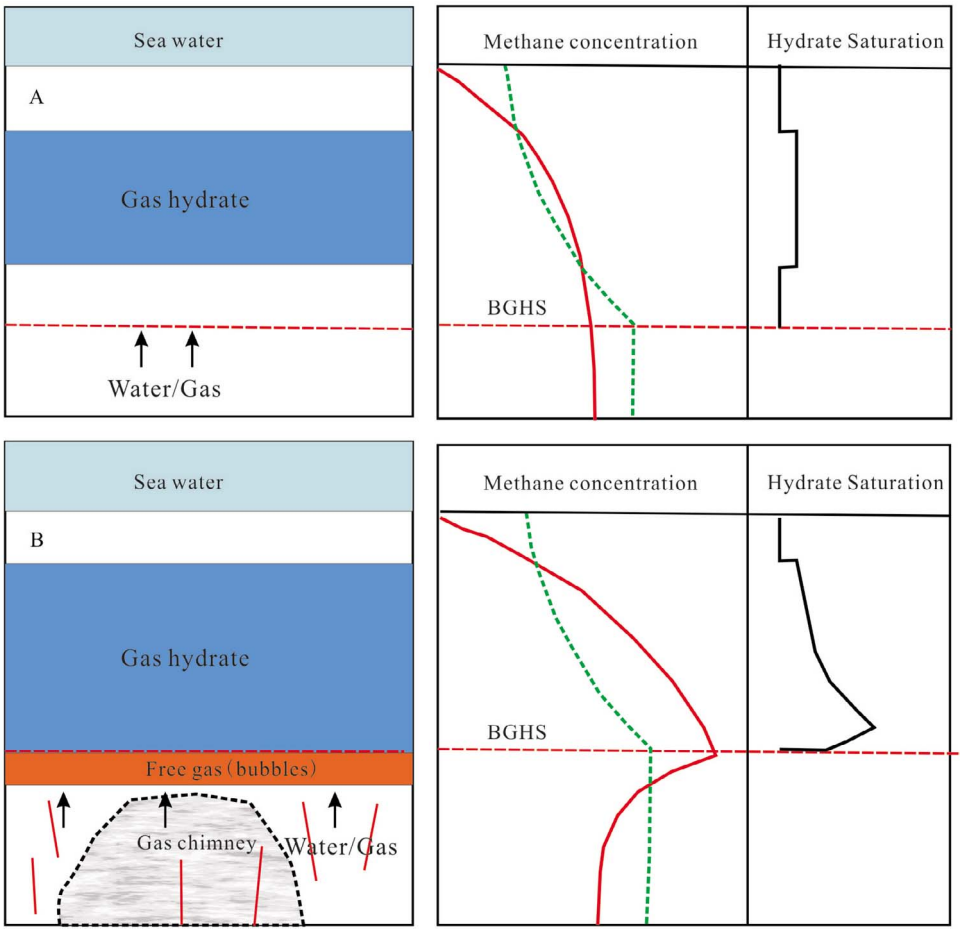

Figure 12. Cartoons showing two formation processes for the gas hydrate petroleum system in the Shenhu area (modified from *Collett et al.* [2009] and *Malinverno et al.* [2008]). (a) the uniform and low gas hydrate saturation is formed by stable and low methane flux above the base of gas hydrate stability zone (BGHS); gas hydrate forms where the concentration of methane (red line) exceeds methane solubility zone (green dashed line); (b) higher gas saturation is formed above the BGHS because high methane flux occurs in the presence of gas chimneys that introduces fluids into the base of the hydrate stability zone from deeper sediments.

velocity assuming an isotropic reservoir, are similar to those obtained from chloride. The Archie's parameters used in the resistivity estimate are a, m and n equal to 1.3, 2.0, and 2.0, respectively. Lower saturations (less than 10%) were measured shallower in the drill hole but may be beyond the resolution of the methods used in our calculations.

[52] The unexpected occurrence of saturation as high as 45% in silt and silty clay sediments may be due to the increase of calcareous nannofossil abundance at the depths of higher gas hydrate saturations. The size of these foraminifera may change the sediment pore shape and size resulting in a decrease in capillary forces and an increase in permeability of the sediments. The abundant foraminifer can increase the secondary porosity space for the nucleation sites for gas hydrate formation.

[53] The distribution of gas hydrate around site SH2 is heterogeneous both laterally and vertically. Gas chimneys and fractures are identified from seismic profiles, which may be the source and transportation, respectively, of methane supply from the deeper sediments. Bright spots and low *P* wave velocity indicate that free gas is trapped below the gas hydrate stability zone with patchy distribution.

[54] A model for the occurrence of gas hydrate in the sediments is proposed, in which low saturations of gas hydrate, possibly in the shallower parts of the drill hole, occur from biogenic methane and low fluid flux in fine-grained sediments, similar to other passive margin settings where low saturations of gas hydrate are found in fine-grained sediments. The higher saturations of gas hydrate just above the BSR are explained by deeper gas chimneys providing a mechanism to increase fluid flux and by possible shoaling of the base of the GHSZ by sedimentation and local canyon migration.

[55] **Acknowledgments.** We would like to thank the science team of the gas hydrate program expedition Guangzhou Marine Geological Survey-1 (GMGS-1). We are grateful to Myung Lee and Tim Collett for calculating gas hydrate saturations by the simplified three-phase equation model and discussing interpretations of the well log data. They provided many ideas about why the gas hydrate saturations are higher in fine-grained sediments in the South China Sea. We thank William Waite, Carolyn Ruppel, and

Hailong Lu, who also discussed their thoughts about why higher gas hydrate saturation can occur in the fine-grained sediments and the models of gas hydrate-bearing sediment in other places. Myung Lee and Bill Dillon provided many helpful comments and suggestions in their review of the paper, which were much appreciated. We would like thank Kathy Rankin for many grammatical improvements. Fang Chen answered our many questions about mineral components at drilling sites, which was very helpful for us to interpret our data. We thank Ray Boswell and an anonymous reviewer and the Associate Editor for their thorough reviews and constructive comments. Our research is supported by the National Basic Research Program (2009CB219505), International Science & Technology Cooperation program of China (2010DFA21740), and National Natural Science Foundation of China (40930845).

References

Archie, G. E. (1942), The electrical resistivity log as an aid in determining some reservoir characteristics, *J. Pet. Technol.*, *5*, 1–8.

Arntsen, B., L. Wensaas, H. Løseth, and C. Hermanrud (2007), Seismic modeling of gas chimneys, *Geophysics*, *72*, SM251–SM259, doi:10.1190/1.2749570.

Arp, J. J. (1953), The effect of temperature on the density and electrical resistivity of sodium chloride solutions, *Trans. Am. Inst. Min. Metall. Pet. Eng.*, *198*, 327–330.

Briais, A., P. Patriat, and P. Tapponnier (1993), Updated interpretation of magnetic anomalies and seafloor spreading stages in the South China Sea: Implications for the Tertiary tectonics of Southeast Asia, *J. Geophys. Res.*, *98*, 6299–6328, doi:10.1029/92JB02280.

Carcione, J. M., and U. Tinivella (2000), Bottom-simulating reflectors: Seismic velocities and AVO effects, *Geophysics*, *65*, 54–67, doi:10.1190/1.1444725.

Carcione, J. M., D. Gei, G. Rossi, and G. Madrussani (2005), Estimation of gas-hydrate concentration and free-gas saturation at the Norwegian-Svalbard continental margin, *Geophys. Prospect.*, *53*, 803–810, doi:10.1111/j.1365-2478.2005.00502.x.

Cartwright, J., M. Huuse, and A. Aplin (2007), Seal bypass systems, *AAPG Bull.*, *91*, 1141–1166, doi:10.1306/04090705181.

Chen, F., X. Su, Y. Zhou, H. F. Lu, G. H. Liu, Z. X. Chen, and C. Y. Chen (2009), Variations in biogenic components of late Miocene-Holocene sediments from Shenhu area in the northern South China Sea and their geological implication (in Chinese with English abstract), *Mar. Geol. Quat. Geol.*, *29*(2), 1–8.

Chen, F., X. Su, H. F. Lu, and Y. Zhou (2010), Gas hydrate formation and sediment analysis since late Miocene in the northern South China Sea (in Chinese), paper presented at Symposium of Deep Sea Research and Geosciences System, Tongji Univ., Shanghai, China.

Clift, P. D., J. Lin, and U. Barckhausen (2002), Evidence of low flexural rigidity and low viscosity lower continental crust during continental break-up in the South China Sea, *Mar. Pet. Geol.*, *19*, 951–970, doi:10.1016/S0264-8172(02)00108-3.

Collett, T. S., and J. Ladd (2000), Detection of gas hydrate with downhole logs and assessment of gas hydrate concentrations (saturations) and gas volumes on the Blake Ridge with electrical resistivity log data, *Proc. Ocean Drill. Program, Sci. Results*, *164*, 179–191.

Collett, T., et al. (2008), Indian National Gas Hydrate Program Expedition01 initial reports: Expedition 01 of the Indian National Gas Hydrate Program from Mumbai, India to Chennai, India; Sites NGHP-01–01 through NGHP-01–21, April 2006–August 2006, Dir. Gen. of Hydrocarbons, Minist. of Pet. and Nat. Gas, Noida, India.

Collett, T. S., C. C. Knapp, A. H. Johnson, and R. Boswell (2009), Natural gas hydrate: A review, *AAPG Mem.*, *89*, 146–219.

Dallimore, S. R., and T. S. Collett (Eds.) (2005), Scientific Results From the Mallik 2002 Gas Hydrate Production Research Well Program, Mackenzie Delta, Northwest Territories, Canada (CD-ROM), *Bull. Geol. Surv. Can.*, *585*, 1–16.

Dallimore, S. R., T. S. Collett, and T. Uchida (1999), Scientific results from JAPEX/JNOC/GSC Mallik 2L–38 gas hydrate research well, MacKenzie Delta, Northwest Territories, Canada, *Bull. Geol. Surv. Can.*, *544*, 403 pp.

Deptuck, M. E., G. S. Steffens, M. Barton, and C. Pirmez (2003), Architecture and evolution of upper fan channel-belts on the Niger Delta slope and in the Arabian Sea, *Mar. Pet. Geol.*, *20*, 649–676, doi:10.1016/j.marpetgeo.2003.01.004.

Dickens, G. R., and M. S. Quinby-Hunt (1994), Methane hydrate stability in seawater, *Geophys. Res. Lett.*, *21*, 2115–2118, doi:10.1029/94GL01858.

Dvorkin, J., M. Parasad, A. Sakai, and D. Lavoie (1999), Elasticity of marine sediments: Rock physics modelling, *Geophys. Res. Lett.*, *26*, 1781–1784, doi:10.1029/1999GL900332.

Ecker, C., J. Dvorkin, and A. Nur (1998), Sediments with gas hydrates: Internal structure from seismic AVO, *Geophysics*, *63*, 1659–1669, doi:10.1190/1.1444462.

Gardner, G. H. F., L. W. Gardner, and A. R. Gregory (1974), Formation velocity and density: The diagnostic basics for stratigraphic traps, *Geophysics*, *39*, 770–780, doi:10.1190/1.1440465.

Gassmann, F. (1951), Uber die elastizitat poroser median, *Vierteljahrsschr. Naturforsch. Ges. Zuerich*, *96*, 1–23.

Gay, A., M. Lopez, P. Cochonat, M. Se'ranne, D. Levache', and G. Sermondadaz (2006), Isolated seafloor pockmarks linked to BSRs, fluid chimneys, polygonal faults and stacked Oligocene–Miocene turbiditic palaeochannels in the Lower Congo Basin, *Mar. Geol.*, *226*, 25–40, doi:10.1016/j.margeo.2005.09.018.

Gay, A., M. Lopez, C. Berndt, and M. Séranne (2007), Geological controls on focused fluid flow associated with seafloor seeps in the Lower Congo Basin, *Mar. Geol.*, *244*, 68–92, doi:10.1016/j.margeo.2007.06.003.

Ginsburg, G., S. Soloviev, T. Matveeva, and I. Andreeva (2000), Sediment grain size control on gas hydrate presence, Sites 994, 995, and 997, *Proc. Ocean Drill. Program, Sci. Results*, *164*, 237–245.

Guo, T. M., B. H. Wu, Y. H. Zhu, S. S. Fan, and G. J. Chen (2004), A review on the gas hydrate research in China, *J. Petrol. Sci. Eng.*, *41*(1–3), 11–20, doi:10.1016/S0920-4105(03)00139-6.

Hadley, C., D. Peters, A. Vaughan, and D. Bean (2008), Gumusut-Kakap Project: Geohazard characterization and impact on field development plans, paper 12554 presented at International Petroleum Technology Conference, Petrol. Nas. Berhad, Kuala Lumpur, Malaysia, 3–5 Dec.

Hamilton, E. L. (1976), Variations of density and porosity with depth in deep-sea sediments, *J. Sediment. Petrol.*, *46*(2), 280–300.

Hansen, J. P. V., J. A. Cartwright, M. Huusew, and O. R. Clausen (2005), 3-D seismic expression of fluid migration and mud remobilization on the Gjallar Ridge, offshore mid-Norway, *Basin Res.*, *17*, 123–139, doi:10.1111/j.1365-2117.2005.00257.x.

Helgerud, M. B., J. Dvorkin, A. Nur, A. Sakai, and T. Collett (1999), Elastic-wave velocity in marine sediments with gas hydrates: Effective medium modeling, *Geophys. Res. Lett.*, *26*, 2021–2024, doi:10.1029/1999GL900421.

Hill, R. (1952), The elastic behaviour of crystalline aggregate, *Proc. Phys. Soc. London, Sect. A*, *65*, 349–354.

Huang, B. J., X. M. Xiao, and M. Q. Zhang (2003), Geochemistry, grouping and origins of crude oils in the western Pearl River Mouth Basin, offshore South China Sea, *Org. Geochem.*, *34*, 993–1008, doi:10.1016/S0146-6380(03)00035-4.

Huang, X., Y. H. Zhu, Z. Q. Lu, and P. K. Wang (2010), Study on genetic types of hydrocarbon gases from the gas hydrate drilling area, the northern South China Sea, *Geoscience*, *24*, 576–580.

Klausner, Y. (1991), *Fundamentals of Continuum Mechanics of Soils*, Springer, London.

Korenaga, J., W. S. Holbrook, S. C. Singh, and T. A. Minshull (1997), Natural gas hydrates on the southeast U.S. margin: Constraints from Full wave form and travel time inversion of wide-angle seismic data, *J. Geophys. Res.*, *102*, 15,345–15,365, doi:10.1029/97JB00725.

Kraemer, L. M., R. M. Owen, and G. R. Dickens (2000), Lithology of the upper gas hydrate zone, Blake ridge: A link between diatoms, porosity, and gas hydrate, *Proc. Ocean Drill. Program, Sci. Results*, *164*, 229–236.

Lee, M. W. (2002), Biot-Gassmann theory for velocities of gas hydrate-bearing sediments, *Geophysics*, *67*, 1711–1719, doi:10.1190/1.1527072.

Lee, M. W. (2008), Models for gas hydrate-bearing sediments inferred from hydraulic permeability and elastic velocities, *U.S. Geol. Surv. Sci. Invest. Rep.*, *2008–5219*, 15 pp.

Lee, M. W., and T. S. Collett (2001), Gas hydrate estimation error associated with uncertainties of measurement and parameters, *U.S. Geol. Surv. Sci. Invest. Rep.*, *2001–52182*, 8 pp.

Lee, M. W., and T. S. Collett (2009a), Gas hydrate saturations estimated from fractured reservoir at Site NGHP-01–10, Krishna-Godavari Basin, India, *J. Geophys. Res.*, *114*, B07102, doi:10.1029/2008JB006237.

Lee, M. W., and T. S. Collett (2009b), Unique problems associated with seismic analysis of partially gas-saturated unconsolidated sediments, *Mar. Pet. Geol.*, *26*, 775–781, doi:10.1016/j.marpetgeo.2008.07.009.

Lee, M. W., and W. F. Waite (2008), Estimating pore-space gas hydrate saturations from well log acoustic data, *Geochem. Geophys. Geosyst.*, *9*, Q07008, doi:10.1029/2008GC002081.

Lee, M. W., D. R. Hutchinson, W. P. Dillon, J. J. Miller, W. F. Agena, and A. B. Swift (1993), Method of estimating the amount of in-situ gas hydrates in deep marine sediments, *Mar. Pet. Geol.*, *10*, 493–506, doi:10.1016/0264-8172(93)90050-3.

Lee, M. W., D. R. Hutchinson, W. F. Agena, W. P. Dillon, J. J. Miller, and B. A. Swift (1994), Seismic character of gas hydrates on the southeastern U.S. continental margin, *Mar. Geophys. Res.*, *16*, 163–184, doi:10.1007/BF01237512.

Lee, M. W., D. R. Hutchinson, T. S. Collett, and W. P. Dillon (1996), Seismic velocities for hydrate-bearing sediments using weighted equation, *J. Geophys. Res.*, *101*, 20,347–20,358, doi:10.1029/96JB01886.

Li, Y. M., X. H. Luo, X. Xu, X. Q. Yang, and X. B. Shi (2010), Seafloor in-situ heat flow measurements in the deep-water area of the northern slope, South China Sea (in Chinese with English abstract), *Chin. J. Geophys.*, *53*(9), 2161–2170, doi:10.3969/j.issn.0001-5733.2010.09.16.

Lindseth, R. O. (1979), Synthetic sonic logs—A process for stratigraphic interpretation, *Geophysics*, *44*, 3–26, doi:10.1190/1.1440922.

Liu, X., and P. B. Flemings (2007), Dynamic multiphase flow model of hydrate formation in marine sediments, *J. Geophys. Res.*, *112*, B03101, doi:10.1029/2005JB004227.

Løseth, H., M. Gading, and L. Wensaas (2009), Hydrocarbon leakage interpreted on seismic data, *Mar. Geol.*, *26*(7), 1304–1319, doi:10.1016/j.marpetgeo.2008.09.008.

Lu, H. F., H. Chen, F. Chen, and Z. L. Liao, (2009), Mineralogy of the sediments from gas hydrate drilling site, Shenhu area, South China Sea (in Chinese with English abstract), *Geol. Res. South China Sea*, *20*, 28–39.

Lu, S., and G. A. McMechan (2002), Estimating of gas hydrate and free gas saturation, concentration, and distribution from seismic data, *Geophysics*, *67*, 582–593, doi:10.1190/1.1468619.

Malinverno, A. (2010), Marine gas hydrates in thin sand layers that soak up microbial methane, *Earth Planet. Sci. Lett.*, *292*, 399–408, doi:10.1016/j.epsl.2010.02.008.

Malinverno, A., M. Kastner, M. E. Torres, and U. G. Wortmann (2008), Gas hydrate occurrence from pore water chlorinity and downhole logs in a transect across the northern Cascadia margin (Integrated Ocean Drilling Program Expedition 311), *J. Geophys. Res.*, *113*, B08103, doi:10.1029/2008JB005702.

Mayall, M., E. Jones, and M. Casey (2006), Turbidite channel reservoirs-key elements in facies prediction and effective development, *Mar. Pet. Geol.*, *23*, 821–841, doi:10.1016/j.marpetgeo.2006.08.001.

Meldahl, P., R. Heggland, A. H. Bril, and P. Groot (2001), Identifying fault and gas chimneys using multi-attributes and neural networks, *Lead. Edge*, *20*, 474–482, doi:10.1190/1.1438976.

Mindlin, R. D. (1949), Compliance of elastic bodies in contact, *J. Appl. Mech.*, *71*, 259–268.

Nimblett, J., and C. Ruppel (2003), Permeability evolution during the formation of gas hydrate in marine sediments, *J. Geophys. Res.*, *108*(B9), 2420, doi:10.1029/2001JB001650.

Pang, X., C. M. Chen, and M. Zhu (2006), A discussion about hydrocarbon accumulation conditions in the Baiyun deep-water area, northern continental slope, South China Sea, (in Chinese), *China Offshore Oil Gas*, *18*, 145–149.

Paull, C. K., and R. Matsumoto (2000), Leg 164 overview, *Proc. Ocean Drill. Program, Sci. Results*, *164*, 1–8.

Paull, C. K., and W. Ussler (1997), Are low salinity anomalies below BSRs a consequence of interstitial gas bubble barriers?, *Eos Trans. AGU*, *78*(46), Fall Meet. Suppl., F339.

Paull, C. K., et al. (Eds.) (1996), *Proceedings of the Ocean Drilling Program, Initial Reports*, vol. 164, Ocean Drill. Program, College Station, Tex.

Paull, C. K., W. Ussler III, T. Lorenson, W. Winters, and J. Dougherty (2005), Geochemical constraints on the distribution of gas hydrates in the Gulf of Mexico, *Geo Mar. Lett.*, *25*, 273–280, doi:10.1007/s00367-005-0001-3.

Pearson, C. F., P. M. Halleck, P. L. McGuire, R. Hermes, and M. Mathews (1983), Natural gas hydrate: A review of in situ properties, *J. Phys. Chem.*, *87*, 4180–4185, doi:10.1021/j100244a041.

Riedel, M., P. E. Long, and T. S. Collett (2006), Estimates of in situ gas hydrate concentration from resistivity monitoring of gas hydrate bearing sediments during temperature equilibration, *Mar. Geol.*, *227*, 215–225, doi:10.1016/j.margeo.2005.10.007.

Ru, K., and J. D. Pigott (1986), Episodic rifting and subsidence in the South China Sea, *AAPG Bull.*, *70*, 1136–1155.

Ruppel, C. (2001), Hydrodynamics of marine methane hydrate reservoirs: Observations and modeling, *Eos Trans. AGU*, *82*(20), Spring Meet. Suppl., Abstract T21A–02.

Ruppel, C., and M. Kinoshita (2000), Fluid, methane, and energy flux in an active margin gas hydrate province, offshore Costa Rica, *Earth Planet. Sci. Lett.*, *179*, 153–165, doi:10.1016/S0012-821X(00)00096-0.

Ruppel, C., R. Boswell, and E. Jones (2008), Scientific results from Gulf of Mexico Gas Hydrates Joint Industry Project Leg 1 Drilling: Introduction and overview, *Mar. Pet. Geol.*, *25*, 819–829, doi:10.1016/j.marpetgeo.2008.02.007.

Schultheiss, P., M. Holland, and G. Humphrey (2009), Wireline coring and analysis under pressure: Recent use and future developments of the HYACINTH system, *Sci. Drill.*, *7*, 44–50, doi:10.2204/iodp.sd.7.07.2009.

Sloan, E. D. (1998), *Clathrate Hydrates of Natural Gases*, 2nd ed., 628 pp., Marcel Dekker, New York.

Tinivella, U., and E. Lodolo (2000), The Blake Ridge bottom-simulating reflector transect: Tomographic velocity field and theoretical model to estimate methane hydrate quantities, *Proc. Ocean Drill. Program, Sci. Results*, *164*, 273–281.

Torres, M. E., et al. (2008), Methane hydrate formation in turbidite sediments of northern Cascadia, IODP Expedition 311, *Earth Planet. Sci. Lett.*, *271*, 170–180.

Tréhu, A. M., D. S. Stakes, C. D. Bartlett, J. Chevallier, R. A. Duncan, S. K. Goffredi, S. M. Potter, and K. A. Salamy (2003), Seismic and seafloor evidence for free gas, gas hydrates, and fluid seeps on the transform margin offshore Cape Mendocino, *J. Geophys. Res.*, *108*(B5), 2263, doi:10.1029/2001JB001679.

Tréhu, A. M., et al. (2004), Three-dimensional distribution of gas hydrate beneath the seafloor: Constraints from ODP Leg 204, *Earth Planet. Sci. Lett.*, *222*, 845–862, doi:10.1016/j.epsl.2004.03.035.

Tréhu, A. M., C. Ruppel, M. D. Holland, G. R. Dickens, M. E. Torres, T. S. Collett, D. Goldberg, and P. Schultheiss (2006), Gas hydrates in marine sediments: Lessons from scientific ocean drilling, *Oceanography*, *19*, 124–142.

Uchida, T., and T. Takashi (2004), Petrophysical properties of natural gas hydrate-bearings and sand their sedimentology in the Nankai Trough, *Resour. Geol.*, *54*, 79–87, doi:10.1111/j.1751-3928.2004.tb00189.x.

Wang, X. J., S. G. Wu, N. Xu, and G. X. Zhang (2006), Estimation of gas hydrate saturation using constrained sparse spike inversion: Case study from the northern South China Sea, *Terr. Atmos. Ocean Sci.*, *17*(4), 799–813.

Wang, X. J., S. G. Wu, S. Q. Yuan, D. W. Wang, Y. B. Ma, G. S. Yao, and Y. G. Gong (2010), Geophysical signatures associated with fluid flow and gas hydrate occurrence in a tectonically quiescent sequence, Qiongdongnan Basin, South China Sea, *Geofluids*, *10*, 351–368, doi:10.1111/j.1468-8123.2010.00292.x.

Winters, W. J., et al. (2010), Physical properties of sediment from the Mount Elbert Gas Hydrate Stratigraphic Test Well, Alaska North Slope, *Mar. Pet. Geol.*, *28*, 361–380, doi:10.1016/j.marpetgeo.2010.01.008.

Wood, W. T., P. L. Stoffa, and T. H. Shipley (1994), Quantitative detection of methane hydrate through high-resolution seismic velocity analysis, *J. Geophys. Res.*, *99*, 9681–9695, doi:10.1029/94JB00238.

Wu, N. Y., S. X. Yang, H. Q. Zhang, J. Q. Liang, H. B. Wang, X. Su, and S. Y. Fu (2008), Preliminary discussion on natural gas hydrate reservoir system of Shenhu area, North Slope of South China Sea, paper presented at 6th International Conference on Gas Hydrates (ICGH 2008), 7 pp., Worldoils, Vancouver, B. C., Canada, 6–10 Jul.

Wu, N. Y., S. X. Yang, H. B. Wang, J. Q. Liang, Y. H. Gong, Z. Q. Lu, D. D. Wu, and H. X. Guan (2009), Gas hydrate-bearing fluid influx sub-system for gas hydrate geological system in Shenhu Area, Northern South China Sea (in Chinese with English abstract), *Chin. J. Geophys.*, *52*(6), 1641–1650.

Wu, N. Y., S. X. Yang, H. Q. Zhang, J. Q. Liang, H. B. Wang, and J. A. Lu (2010), Gas hydrate system of Shenhu area, northern South China Sea: Wireline logging, geochemistrical results and preliminary resources estimates, paper 20485 presented at Offshore Technology Conference, Houston, Tex., 3–6 May.

Wu, S. G., G. X. Zhang, Y. Y. Huang, J. Q. Liang, and H. K. Wong (2005), Gas hydrate occurrence on the northern slope of the South China Sea, *Mar. Pet. Geol.*, *22*, 403–412, doi:10.1016/j.marpetgeo.2004.11.006.

Wu, S. G., X. J. Wang, H. K. Wong, and G. X. Zhang (2007), Low-amplitude BSRs and gas hydrate concentration on the northern margin of the South China Sea, *Mar. Geophys. Res.*, *28*, 127–138, doi:10.1007/s11001-007-9020-y.

Wu, S. G., D. D. Dong, S. X. Yang, G. X. Zhang, Z. J. Wang, Q. P. Li, J. Q. Liang, Y. H. Gong, and Y. B. Sun (2009), Genetic model of the hydrate system in fine-grained sediments in the northern continental slope of South China Sea (in Chinese with English abstract), *Chin. J. Geophys.*, *52*(7), 1849–1857.

Wyllie, M. R. J., A. R. Gregory, and G. H. F. Gardner (1958), An experimental investigation of factors affecting elastic wave velocities in porous media, *Geophysics*, *23*, 459–493, doi:10.1190/1.1438493.

Xu, H. N., S. X. Yang, X. D. Zheng, M. J. Wang, and J. S. Wang (2010), Seismic identification of gas hydrate and its distribution in Shenhu area, South China Sea (in Chinese with English abstract), *Chin. J. Geophys.*, *53*(7), 1691–1698.

Xu, W. Y. (2004), Modeling dynamic marine gas hydrate systems, *Am. Mineral.*, *89*, 1271–1279.

Xu, W. Y., and C. Ruppel (1999), Predicting the occurrence, distribution, and evolution of methane gas hydrate in porous marine sediments, *J. Geophys. Res.*, *104*, 5081–5095, doi:10.1029/1998JB900092.

Xu, W. Y., R. P. Lowell, and E. T. Peltzer (2001), Effect of seafloor temperature and pressure variation on methane flux from a gas hydrate layer: Comparison between current and late Paleocene climate conditions, *J. Geophys. Res.*, *106*, 26,413–26,423, doi:10.1029/2001JB000420.

Yang, S. X., H. Q. Zhang, N. Y. Wu, X. Su, P. Schultheiss, M. Holland, G. Zhang, J. Liang, J. Lu, and K. Rose (2008), High concentration hydrate in disseminated forms obtained in Shenhu area, North Slope of South China Sea, paper presented at 6th International Conference on Gas Hydrates (ICGH 2008), 10 pp., Worldoils, Vancouver, B. C., Canada, 6–10 Jul.

Yuan, T., R. D. Hyndman, G. D. Spence, and B. Desmons (1996), Seismic velocity increase and deep-sea gas hydrate concentration above a bottom-simulating reflector on the northern Cascadia continental slope, *J. Geophys. Res.*, *101*, 13,655–13,671, doi:10.1029/96JB00102.

Zhang, G. X., Y. Y. Huang, Y. H. Zhu, and B. H. Wu (2002), Prospect of gas hydrate resources in the South China Sea, (in Chinese), *Mar. Geol. Quat. Geol.*, *22*(1), 75–81.

Zhang, H. Q., S. X. Yang, N. Y. Wu, X. Xu, H. Melanie, S. Peter, R. Kelly, B. Heather, H. Gary, and GMGS-1 Science Team (2007), Successful and surprising results for China's first gas hydrate drilling expedition, in *Fire in the Ice*, *Methane Hydrate Newsl.*, Fall issue 6–9, Natl. Energy Technol. Lab., U.S. Dep. of Energy, Washington, D. C.

Zhu, M. Z., S. Grahamb, X. Pang, and T. McHargue (2010), Characteristics of migrating submarine canyons from the middle Miocene to present: Implications for paleoceanographic circulation, northern South China Sea, *Mar. Pet. Geol.*, *27*, 307–319, doi:10.1016/j.marpetgeo.2009.05.005.

Zhu, W. L., B. J. Huang, L. J. Mi, R. W. T. Wilkins, N. Fu, and X. M. Xiao (2009), Geochemistry, origin, and deep-water exploration potential of natural gases in the Pearl River Mouth and Qiongdongnan basins, South China Sea, *AAPG Bull.*, *93*, 741–761, doi:10.1306/02170908099.

Y. Guo and S. Yang, Guangzhou Marine Geological Survey, MLR, Guangzhou 510760, China.

D. R. Hutchinson, U.S. Geological Survey, 384 Woods Hole Rd., Woods Hole, MA 02543, USA.

X. Wang and S. Wu, Key Laboratory of Marine Geology and Environment and Institute of Oceanology, Chinese Academy of Sciences, Qingdao 266071, China. (wangxiujuan@qdio.ac.cn)